UNIVERSIDAD AUTÓNOMA DE NUEVO LEÓN

FACULTAD DE CIENCIAS QUÍMICAS

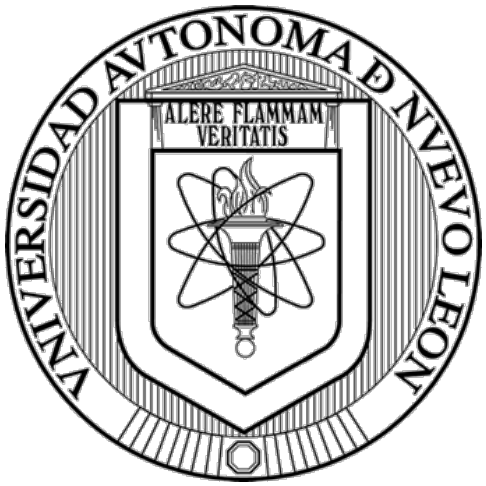

HYBRID SOLAR CELLS OF PYRITE-BASED/POLY(3- HEXYLTHIOPHENE) CORE/SHELL NANOWIRES

POR

M.C. MARÍA FERNANDA RETANA BETANCOURT

Como requisito parcial para obtener el Grado de DOCTOR EN CIENCIAS con Orientación en Química de los Materiales

Junio, 2021

HYBRID SOLAR CELLS OF PYRITE-BASED/POLY(3- HEXYLTHIOPHENE) CORE/SHELL NANOWIRES

Los miembros del comité de tesis aprobamos la tesis realizada por la alumna María Fernanda Retana Betancourt, matrícula 1458498, como opción al grado de Doctor en Ciencias con Orientación en Química de los Materiales.

_____

Dra. Thelma Elizabeth Serrano Quezada

Directora de Tesis

_____

Dra. Ma. Idalia Gómez de la Fuente

Co-Directora de Tesis

_____

Dr. Boris I. Kharisov

_____

Dra. Yolanda Peña Méndez

_____

Dra. María de Jesús de la Garza Galván

_____

Dra. Dena Pourjafari Nokandeh

_____

Dra. Ma. Elena Cantú Cárdenas

Sub-directora de Estudios de Posgrado

FUNDING

The present research received funding by el Consejo Nacional de Ciencia y Tecnología (CONACYT) through the grant PN150.

Also, la Universidad Autónoma de Nuevo León sponsored this project by Programa de Apoyo a la Investigación Científica y Tecnológica (PAICYT) grant IT1088-19.

Abstract

María Fernanda Retana Betancourt **Graduation date: June, 2021**

Universidad Autónoma de Nuevo León, Facultad de Ciencias Químicas

Study Title: Hybrid Solar Cells of Pyrite-Based/Poly(3-Hexylthiophene) Core/Shell Nanowires

Page numbers: 110 **Candidato para el grado de Doctor en Ciencias con Orientación en Química de los Materiales**

Study Field: Nanochemistry and hybrid solar cells

Purpose and Study Method: Iron pyrite (FeS_2) is a candidate semiconductor in the development of high efficiency photovoltaic devices. A real commercialization of solar cells leads to fabricate photovoltaic devices of earth-abundant and low-cost materials. The FeS_2 shows strong optical and electrical properties for solar energy application. Although the highest efficiency for a pyrite-based hybrid solar cell is 3%. The poor performance of the hybrid solar cells is explained by surface passivation and the presence of isomorphs. Raised strategies involve the coupling with wide-bandgap inorganic semiconductor (ZnO) to form p-n heterojunction while the coupling with conducting polymers (Poly(3-hexylthiophene) can form a donor-acceptor interface increasing optical and electrical properties. Therefore, it is the aim of this work the synthesis of photoactive materials of FeS_2, ZnO and the polymeric matrix of poly(3-hexylthiophene) in order to study their optical, structural and morphological behavior for their potential application in hybrid solar cells.

Contributions and Conclusions: One-dimensional poly(3-hexylthiophene) and ZnO thin films were obtained by electrochemical method. The electrochemical parameters influence the morphology and sizes tuning the optical properties, which it enables to obtain multifunctional nanomaterials. The conversion of nanorods into a tubular morphology is possible due to the defects and metastability of ZnO. The hollow structures allow the coupling with FeS_2 nanoparticles and offer the possibility to increase the optical absorption due to the high surface area and exciton confinement. The iron pyrite nanoparticles were obtained using complexing agents for the very first time. Air-stable FeS_2 show stability for 21 days without special storage conditions. The semiconductors obtained exhibit suitable optical, structural and morphological properties for solar energy conversion.

DIRECTOR'S SIGNATURE: _____

CO-DIRECTOR'S SIGNATURE: _____

Table of contents

Table of Figures

List of Abbreviations

PV	Photovoltaics
a-Si	Amorphous silicon
Cu_2MSnS_4	Quaternary copper chalcogenide
FeS_2	Pyrite
ZnO	Zinc oxide
ZnS	Zinc sulfide
P3HT	Poly(3-hexylthiophene)
PCBM	Phenyl-C61-butyric acid methyl ester
FeZnS	Iron zinc sulfide
$FeCdS_3$	Iron cadmium sulfide
HSC	Hybrid Solar Cells
Al	Aluminum
Ag	Silver
Au	Gold
PEDOT:PSS	Poly(3,4-ethylenedioxythiophene) polystyrene sulfonate
ITO	Indium Tin Oxide
EQE	External Quantum Efficiency
HOMO	Highest Occupied Molecular Orbital
LUMO	Lowest Unoccupied Molecular Orbital
Eg	Bandgap
eV	Electronvolt
VB	Valence Band
CB	Conduction Band
GaAs	Gallium arsenide
CdTe	Cadmium Telluride
$S \cdot cm^{-1}$	Siemens per cm
1D	One-dimensional
CuO	Copper oxide
CdS	Cadmium sulfide
CdSe	Cadmium selenide
PbS	Lead sulfide
Pt	Platinum
DC	Direct Current
AC	Alternating Current
A	Ampere
V	Volt
AAO	Anodic Aluminum Oxide
CoS_2	Cobalt sulfide
$FeSe_2$	Iron selenide
C	Carbon
Sb_2S_3	Antimony trisulfide
PEDOT	Poly(3,4-ethylenedioxythiophene)
SEM	Scanning electron microscopy

Fe_2MS_4	Ternary iron sulfide
kW	KiloWatt
¢	USD cent
$	USD dollar
MW	Microwave
KOH	Potassium hydroxide
AgCl	Silver chloride
CA	Chronoamperometry
pH	Power of hydrogen
nm	Nanometer
MPA	Mercaptopropionic acid
GHz	GigaHertz
N_2	Nitrogen
s	Seconds
LSV	Linear Sweep Voltammetry
CV	Cyclic Voltammetry
Ω/sq	Ohm per square
WE	Working electrode
RE	Reference electrode
CE	Counter-electrode
UV-vis	Ultraviolet-visible spectroscopy
FT-IR	Fourier-transform spectroscopy
XRD	X-Ray Diffraction
EIS	Electrochemical Impedance Spectroscopy
V_{oc}	Open circuit voltage
J_{sc}	Shor-circuit current
FF	Fill Factor
V_{max}	Maximum voltage
J_{max}	Maximum current
DTA-TGA	Differential thermal analysis and thermogravimetric analysis
FE-SEM	Field Emission Scanning Electron Microscopy (FE-SEM):
TEM	Transmission electron microscopy
$TBaPF_6$	Tetrabutylammonium hexafluorophosphate
$Zn(OH)_2$	Zinc hydroxide
O_2	Oxygen
E	Potential
V_{Zn}	Zinc vacancy
O_i	Oxygen interstitial
Zn_i	Zinc interstitial
V_o	Oxygen vacancy
ZnS	Zinc sulfide
FeS	Iron sulfide

Chapter I

Introduction

1. Hybrid solar cells in the modern world

Green and low-cost energy sources have become an important issue due to the global warming that causes an increase of carbon dioxide concentration. In order to respond the increasing energy demand, renewable energy technologies have been studied extensively. It is the aim of this work the solar photovoltaic technology, which is centered in the conversion of solar energy into electrical through solar cells.

The most promising devices in solar cells includes nanocrystal sensitized solar cells, all-inorganic nanocrystal solid solar cells and hybrid solar cells, including different configurations and semiconductor nanocrystals within them. It is important to remark the current research in photovoltaics (PV) is focused on offering sustainable and real technologies, it means that the photovoltaic devices should consist of semiconductors with high affinity to the environment but at the same time, manufacturing and commercialize process cannot be so expensive [1-3].

Hybrid photovoltaic devices are based on the combination of organic and inorganic semiconductors. This hybrid device allows the possibility to develop easily solar panels due to the easy fabrication process and less production cost [4]. While conducting polymers contribute to the flexibility, effective hole transportation, conductivity and versatile of the device, the size and shape of inorganic semiconductors can tune

characteristics as the band gap. Moreover, the use of earth abundant semiconductors provides a sustainable option as energy source [5].

Recent research focus on the use of earth-abundant photoactive semiconductors. This group includes materials as amorphous silicon (a-Si), quaternary-structured semiconductors, Cu_2MSnS_4 (M = Fe, Zn, Ni and Mn) [6-7], and FeS_2 (pyrite) [8], mainly. Wadia *et al.* in 2009, reported a study about 23 semiconductors and their feasibility to provide enough electricity [9]. FeS_2 gained interest as a potential non-toxic absorber material due to its outstanding optical properties.

1.2. FeS_2, the most suitable semiconductor for solar cells applications

FeS_2 (pyrite) is an earth-abundant, non-toxic and low cost semiconductor. It is one of the most promising material for solar applications due to its band gap of 0.95 eV, charge mobility of 360 $cm^2\ V^{-1}\ s^{-1}$, high absorption coefficient ($\alpha > 10^5\ cm^{-1}$, two orders of magnitude greater than the absorption coefficient of silicon), high carrier mobility and a Shockley-Queisser limit around 31% [10-11]

Iron pyrite is particularly suitable for large scale, roll to roll deposition or ink-jet printing on flexible substrates. FeS_2 nanocrystals may offer low-cost devices since the high absorption coefficient allows to fabricate thin absorber layers (<20 nm). Despite the theorical optoelectronic properties, FeS_2 hybrid solar cells have not overcome the

energy conversion efficiency of 3% [12]. Challenges are present during the synthesis as the presence of unwanted isomorphs and surface defects, these two situations are responsible for the low photovoltage of the devices [13-14]

Some approaches to improve FeS_2 solar cells performance are the coupling with wide-band gap semiconductors (e.g. ZnO, ZnS) or conducting polymers, e.g. poly(3-hexylthiophene) (P3HT) and phenyl-C61-butyric acid methyl ester (PCBM) [15-16]. Recently, the study of iron-based ternary chalcogenides (FeZnS [17] , $FeCdS_3$ [18]) has been implemented as a new pathway to offer absorber materials with similar optical and electrical properties as iron pyrite.

1.3. Nanowires in Hybrid Solar Cells

Nanowire photovoltaic is a new strategy to build solar cells with high efficiency at low-cost. In addition, the one-dimensional morphology may decrease the low photovoltage in the devices, reduce the loss of energy due to the light reflection and enhance the light-scattering effect. However, low-efficiency devices have been obtained for homogeneous nanowires compared to their bulk-counterparts. As an alternative to this challenge, heterogeneous nanowires provide the combination of the optoelectronic properties of two or more semiconductors in one system, which influences their performance in solar cells [19].

There are three different types of heterogeneous nanowires although core/shell nanowires present major advantages as a direct charge transport, more efficient and controllable charge separation, while the charge collection can be enhanced due to the coupling of two inorganic semiconductors. Adding a third component such as a conducting polymer, acting as hole transport material, forms the donor-acceptor interface and enhances the charge separation [20-21]. Moreover, the high surface area increases the interface between inorganic and organic molecules that may increase the electronic mobility around the hybrid solar cell.

1.4. Aim of the Study

The aim of this work is to obtain cheaper and efficient hybrid thin films based on Fe-based semiconductors and poly(3-hexylthiophene). The study of the photovoltaic properties will offer an opportunity to extend the knowledge about pyrite and its composites in order to increase their use commercially in the market.

Chapter II

Background Knowledge and Literature review

2.1. Hybrid solar cells

Hybrid solar cells (HSC) emerged as an alternative solution for energy demand since Si modules cost and availability represents a disadvantage for their future commercial process. HSC combine inorganic and organic materials in order to join their unique optical, structural and electrical properties. HSC involves the use of inorganic nanoparticles (a semiconductor type “n”) and a conducting polymer (a semiconductor type “p”) [22-23].

The basic structure of a HSC consists at least of four layers which are cathode, a metal of low work function (Al, Ag, Au, etc.) that allows the electrons transports between conduction band and metal. The hole transport layer, usually PEDOT:PSS due to its transparency, mechanical flexibility and thermal stability. Active layer, the principal layer in HSC since here occurs the absorption of light, diffusion and recombination of excitons and charge carrier diffusion. The anode also consists of a conductive metal and finally, the suitable substrate for HSC is ITO (Indium Tin Oxide) due to its conducting properties and transparency that allows light passes through until active layer [24]. Figure 1(a), illustrates the structure of HSC.

Interfacial charge separation plays an important role at the improvement of efficiency inside the HSC. Parameters as charge separation that occurs in this interface, some of them are interface area, the nominal interfacial driving energy, the morphology of the

interfaces/domains, the interfacial layer/molecules/bridges, the crystallinity of the components, the mixture homogeneity, and the migration of separated charges from the interfaces govern this characteristic, where their influence increase or decrease the photovoltaic conversion efficiency [25].

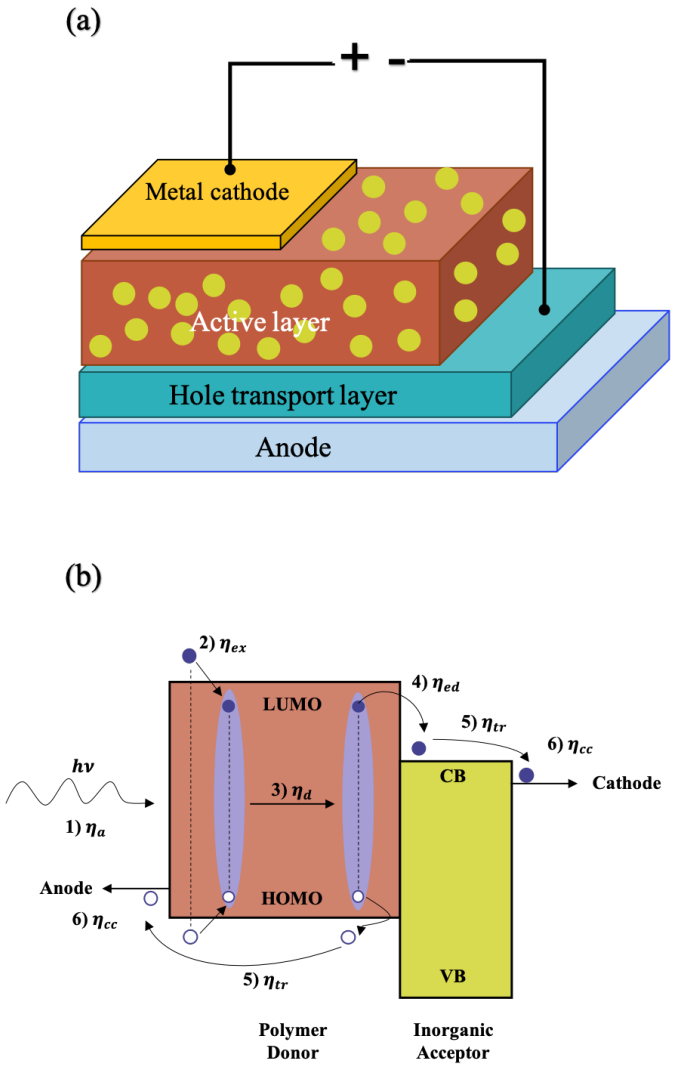

Figure 1. Schematic illustration of (a) HSC structure and (b) its working principle.

2.1.2 Basic Working Principle

Once the polymer and inorganic nanocrystal are combined into a heterojunction device, polymers serve as the electron donor and the hole acceptor, while the inorganic crystal act as the electron acceptor and the hole donor. The importance of the interface is due to here occurs the whole process of light absorption.

The fundamental of the processes of the photovoltaic effect in HSC is shown in Figure 1(b). In literature is described theoretically 5 or 6 main steps, which affect the external quantum efficiency (EQE). EQE is defined as the percentage of the number of charge carriers collected at the electrode under short-circuit conditions to the number of photons incident on the device [26]. It can be expressed by the equation 1:

$$EQE = \eta_a \, x \, \eta_{ex} \, x \, \eta_{diff} \, x \, \eta_{ed} \, x \, \eta_{tr} \, x \, \eta_{cc} \quad (1)$$

Where:

1) **Photo absorption yield (η_a)** is determined mainly by the optical absorption coefficient and thickness of the photoactive layer. Excitons are generated in both polymers and inorganic nanocrystals. Although the excitons formation depends on the dielectric constant and the binding energy, thus it's easier for inorganic nanocrystals to form excitons.
2) **Exciton diffusion (η_{diff})** occurs to the Donor-Acceptor (DA) interface. This

process is vital since when excitons do not reach the interface, they decay to the ground state (recombination process). So, this process is governed by the exciton diffusion length (L_D) and distance between photoexcitation location and DA interface (L_I), where $L_I \leq L_D$.

3) **Efficiency of exciton dissociation (η_{ed})** into free carriers. The energy to dissociate excitons is provided by the energy offset between Lowest Unoccupied Molecular Orbital (LUMO) level of the polymer and the conduction band (CB) of the nanocrystal. Likewise, the Highest Occupied Molecular Orbital (HOMO) level of the polymer and the valence band (VB) of the nanocrystal is required to transport holes.
4) **Carrier transport efficiency (η_{tr})** occurs in two pathways. Hole transfer is made by the polymer and the nanocrystal. While the electron transfer is provided only by the acceptor phase.
5) Finally, **the charge collection efficiency (η_{cc})** occurs when the free carriers (electrons and holes) reach the electrodes. Then, electrons and holes are collected by the electrodes and charge extraction takes place [27-29].

2.1.3 Photoactive layer configuration

Since the donor-acceptor interface is crucial for a better performance of the solar cell, the photoactive configuration have a significant role and can be fabricated in three different configurations, their description is right below and illustrated in Figure 2:

a) **Planar bilayer:** coatings of distinctive film of donor polymer over an inorganic acceptor layer.

b) **Bulk heterojunction:** in a first-step conductive polymer and inorganic semiconductor are mixed together, and then deposited on a conductive and transparent substrate to form the active layer.

c) **Ordered heterojunction layer:** ordered heterojunction are fabricated infiltrating nanomaterials during or after polymerization in ordered arrays as nanorods and nanowires. Although, the carrier transportation and surface area show an enhancement [30].

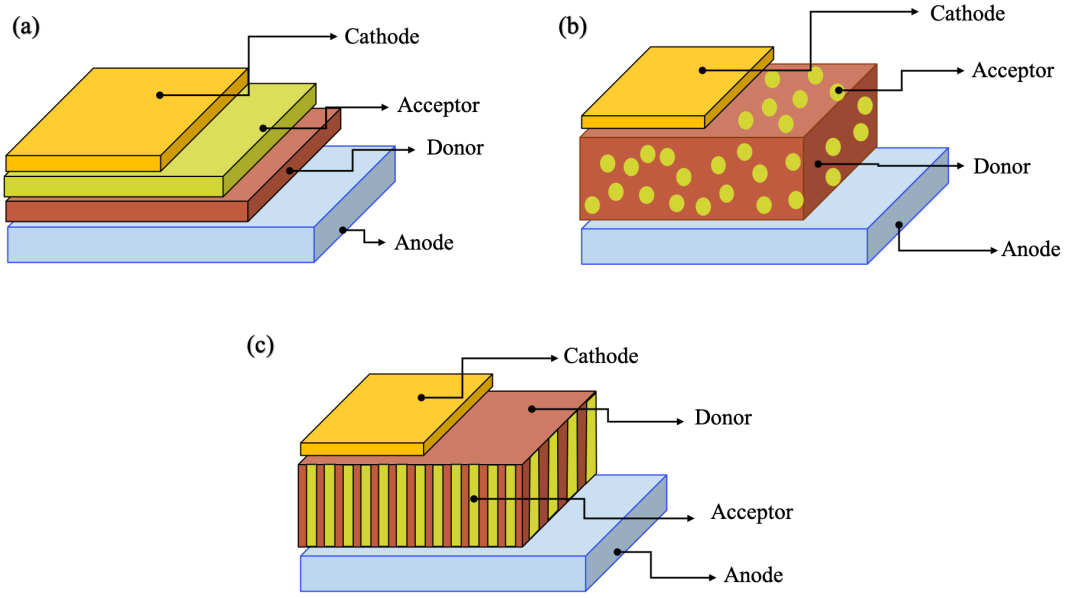

Figure 2. Schematic of various architectures of hybrid solar cells. (a) Planar bilayer, (b) Bulk heterojunction and (c) Ordered heterojunction layer.

Thickness is another crucial parameter for thin films different values of thickness have been reported although most of the papers agree that the thickness between 100-300

nm is enough to absorb light. It could be thought a thicker active layer would absorb more light although the charge transport and collection will be negatively affected [31].

2.2. Materials of HSC

The photovoltaic effect is performed by a material that covered two “simple” criteria. This material is capable to absorb sunlight, generating free charges, and it must be able to transport the carriers to the contact, to extract them and convert the light into work. These criteria are only fulfil by the semiconductors materials and are the only materials used for solar cells.

It is considered a semiconductor material when there is a gap between the HOMO, which is analogous to the highest energy filled called valence band, and the LUMO, its analogous is called conduction band. The energy separation between both orbitals or bands is called energy gap, Eg. The size of Eg influences the electronic and optical properties. Commonly, semiconductors bandgap ranges from 0.5 eV to 3.5 eV [32]. The main differences between inorganic and organic semiconductors lie in their electronic structures. The mechanisms and properties of each one are described in detail in the following sections.

2.2.2. Inorganic Nanocrystals

In inorganic solid crystals, electrons are promoted from the VB into the CB. This promotion can occur by two mechanisms: by the absorption of a photon, or by injecting an electron from a higher energy state into the CB. Since electrons in the CB are free to move through the crystal, an electron will diffuse between these states, or drift in an electric field. Similarly, positive charges (holes) are free to move through the VB. It is this conductance after an external stimuli that gives these materials their name of semiconductors.

The light absorption process in semiconductors has an energy threshold. The value of this threshold is the Eg. Only photons with energies greater than or equal to the band gap energy can induce an electronic transition in the semiconductor. Additionally, using different materials is to fabricate multiple p-n junctions to cover the maximum possible of the solar spectrum. According to the Shockley-Queisser limit the maximum theoretical solar conversion efficiency for a single p-n junction photovoltaic cell is achieved at a bandgap of 1.34 eV [33]. Silicon with a band gap approximately of 1.1 eV covers the 90 % of the solar spectrum although the payback of this kind of solar cells is too high. Other popular materials are GaAs, CdTe, etc unfortunately the have similar problems as the silicon solar cells. As the solar energy production increases, research groups focus on studying materials with adequate band gap (range of 1.1 eV to 1.7 eV), high thermal and chemical stability, abundant on the earth's crust and low-cost production [34].

2.2.3 Polymer Donors

Electrically conducting polymers have become an important alternative material to their inorganic counterparts in the field of renewable energy. The conducting polymers have been synthesized by a number of methods and exhibit properties as low-cost, light weight, easy processability, easy-to-control shape and morphology, flexibility and the most interesting property conductivity as high as 10^3 to 10^4 $S \cdot cm^{-1}$ [35].

Addressing the conducting mechanism, it is important to describe the molecular structure of conducting polymers since on it arises their semiconducting properties. Conducting polymers are conjugated polymers that possess alternating a single localized bond (σ), which forms a strong chemical bond, and double localized (π) bond, which is weaker. This means chemical bonds between two atoms involving one or two pairs of shared electrons. The delocalized electrons in the second pair move along the carbon chain allowing the electron flow through optical and electronic interactions [34,36]. The π-orbitals (bonding) of the organic molecules comprises the valence band, surrounding HOMO, while the π^*-orbitals (antibonding) is surrounded by the LUMO. The energy gap between the HOMO and LUMO is called also bandgap, Eg. It is important to take into account, doping of the semiconducting polymers affect their electrical conductivity since introduces electronic states in the bandgap called polarons or bipolarons [36-37].

In literature is possible to find a variety of works dedicated to conjugated polymers. Polythiophenes derivatives are the most investigated and representative conducting polymers for solar cells. Important characteristics of these polymers are: optical properties can be tuned by the alkyl side chain that also, determines the solubility [38]. The band gap can vary from 1 to 3 eV, easy to fabricate thin films and high stability. A popular donor polythiophene derivative is the poly(3-hexylthiophene) (P3HT). Its advantages are the molecular simplicity, solubility, higher hole mobility, and a band gap of 1.9 eV [39].

Once the semiconductor materials are selected to fabricate the hybrid solar cells, it is important to consider the morphology since it can be a parameter that can improve the performance of these devices.

2.3. Nanowire Solar Cells

One-dimensional (1D) nanomaterials are promising candidates to improve the performance of solar cells due to their anisotropic properties and characteristics as their transparency and conductivity that provides enough interspace for the penetration of incident light; surface area that enables the charge generation, separation and collection; direct charge transport and low electrical resistance [40].

The morphologies for 1D nanomaterials include nanorods, nanobelts, nanotubes, nanofibers, nanopillars, nanowires and so on. The most common nanorods and nanowires can be distinguished by their aspect ratio (length/diameter). Some authors mark an aspect ratio more than 1000 for nanowires and for nanorods from 3 to 5, some other authors considered nanowires aspect ratio higher than 10 and nanorods below this value [41].

Semiconductor nanowires have been fabricated in a wide variety of materials including the popular Si, metal oxides such as ZnO, CuO, chalcogenides as CdS, CdSe, PbS, ZnS, and polymer/carbon nanowires combination. Particularly, polymers in radial p-n junctions may improve the optical absorption and carrier collection compared to the conventional planar p-n junction solar cell geometry. Moreover, the hole mobility can be enhanced several times by the vertical arrangement [42].

1D nanostructures are potential materials for the high efficiency photovoltaic (PV) devices with low cost since are the smallest dimension structure. They can efficiently transport electrical carrier due to diffuse light scattering, short collection lengths of minority carriers that are radially separated and collected normal to the light absorption direction, flexibility, and the presence of anti-reflection and light trapping effect to improve optical absorption [43-44]. In this regard, an important concept when 1D solar cells architectures offer the advantage of the orthogonalization of the light absorption and carrier collection directions, which it is possible due to the radial geometry of p-n

junctions [44].

These benefits of the nanowires geometry within solar cells are described in detail below and shown in Figure 3(a):

a) **Absorption:** once the light of the sun is absorbed by the photoactive layer, different loss mechanisms may occur. The first loss is due to reflection and the second one is the transmission. To improve absorption, the geometry of nanowires offer an antireflection coating and light-trapping schemes. The light trapping is provided by the periodic array of the nanowires through the solar cell.
b) **Exciton formation:** occurs after the absorption of incident sunlight. The loss mechanism is carrier relaxation when the energy is lost as heat due to the carrier-phonon coupling. To reduce this heat loss is to choose a material with optimal bandgap or multiple and complementary materials to form single-junction or multijunction solar cells.
c) **Carrier separation:** new charge separation mechanism can be provided by the nanowires. The quantum confinement along the length can separate electrons and holes without dopants while along the radius increases the defect tolerance.
d) **Carrier collection:** in this process carriers must diffuse to the contacts. The geometry improves the carrier collection efficiency due to the faster band conduction [45-46].

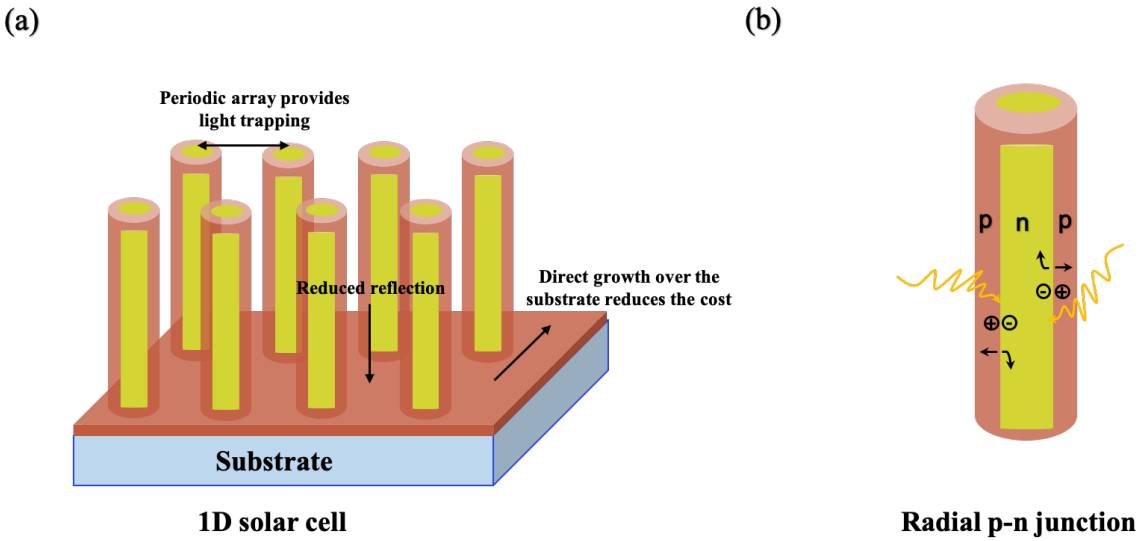

Figure 3. Schematic illustration of core/shell solar cells. (a) Benefits of the nanowire geometry and (b) photovoltaic response in radial junction.

Unlike thin films solar cells, where for high efficiency the active materials have to be thick enough to improve the absorption of the incident photons, 1D materials exhibit the possibility to achieve thin layers grown or transferred to low cost substrates making attractive to commercialize.

2.4. Core/Shell Nanostructures

The pursuit of functional materials with outstanding properties that improve the current electronic, optoelectronic, and electromechanical devices, leads to the interest for such structures as the 1D nanomaterials, since exhibit unique chemical and physical properties for solar energy harvest, conversion and storage.

Heterostructuring has become another important tool in the design of novel nanomaterials that provides new functionalities and enhanced the mentioned devices. Heterojunctions in nanowires and nanorods geometry are not limited to the lattice match. 1D heterostructures include cross-stacked, bilayer, multi-segmented, branched structures and core/shell structures [47-48].

The combination of inorganic and organic materials in 1D heterostructures present numerous factors that benefit their use in HSC. The factors include the colloidal stability by surface passivation, reducing surface tension even affecting the solubility in solution, which provides an answer for the issue about solubility of conducting polymers that stop the further applications. In addition, organic nanostructures provide to the heterostructure system the easy processing and addressing of individual nanostructures. Thus, they are easy to scale up. On the other hand, for hybrid nanomaterials, complexity and functionality of 1D framework can be enhanced. Moreover, the interaction among organic and inorganic phases creates a synergy [48-49].

Core/shell and core/multishell structures nanowires and nanorods consist in two or more conformal shell wrapped around a crystalline core of a different material. The growth of a shell or multishell around the core entails advantages such as [50]:

- The **surface passivation** of the channel, defects in the surface or interface affect the lifetime of minority carriers. The epitaxial growth prevents these defects get active.

- **Thermoelectricity and waveguiding**, shells provide enhanced carrier confinement in the core, reducing surface/interface scattering and shielding them by surface disorder, which increases electrical conductivity. While phonons are scattered by surface disorder, which decreases the thermal conductivity. Moreover, low refraction index shells improve the confinement of phonons promoting waveguiding inside the core in light-emitting devices.

- **Quantum confinement**, controlling optoelectronic properties by controlling diameter size.

- **Surrounding-gate architecture**, enhancement in the electrical properties due to interface between both materials.

In addition, core/shell nanowires and nanorods show a photovoltaic response (Figure 3(b)), when the electron-hole pairs are generated under light illumination and carriers can be separated. In radial structures, as the core/shell, allows a short carrier diffusion range and a large interface for efficient carrier separation and transport [51].

2.5. Electrochemical Method and Concepts

Electrochemistry is defined as the branch of chemistry that examines the phenomena resulting from combined chemical and electrical effects. There are only three principal sources for the analytical signal - potential, current, and charge. Electrochemistry involves a several methods as the coulometry, voltammetry, chronolectric methods and electrogravimetry: weights of substance which was distributed owing to passage of certain current force through a solution.

The experimental procedure in this thesis are carried out by electrodeposition through techniques as cyclic voltammetry and chronoamperometry. Electrodeposition is defined as the growth of a film that consist in the formation of metallic or semiconducting coatings on conducting substrates. This process begins with metal ions in a suitable solvent via charge transfer process. Electrodeposition exhibits unique characteristics as it does not require vacuum environment, minimal capital investment and easy to scale-up. Experiments can be performed at low temperatures (0-100 ºC) and the film growth can be controlled by the potential or current applied [52-53].

The electrochemical setup consists typically of three-electrodes:

a) Working electrode (WE): is the most important component in the electrochemical cell since on it occurs the reaction of interest. The most commonly used working electrode materials are platinum, gold, carbon among

others. Chemically modified electrodes are employed for the synthesis and analysis of organic and inorganic materials. These electrodes are ITO or FTO slide glass, Si wafers, etc

b) Reference electrode (RE): is a stable electrode with a well-known electrode potential. It provides a stable potential controlled of the working electrode and it is used to determine the other half's cell potential. They are classified as aqueous, calomel, non-aqueous and own-constructing.

c) Counter-electrode (CE): is also called auxiliary electrode. This electrode is used to complete the electrical circuit without compromising the stability of the reference electrode by passing current over it. The counter-electrode potential is not measured in the three-electrode system and is adjusted to balance the reaction on the working electrode. These electrodes are often made of inert material such as gold, platinum or carbon being Pt widely used due to its resistance to oxidation.

d) Supporting electrolyte: inert salts added to the solution to increase solution conductivity between electrodes and eliminate migration of the analyte to the working electrode and do not take part in any reaction.

In this work is used as WE anodic aluminum oxide (AAO). The template-assisted electrodeposition is based on the growth of nanostructures under current or potential control. Diameter and length of 1D can be tuned by AAO pore size and by the time of electrodeposition respectively [54-57].

The electrochemical cell setup and the structure of the AAO membrane is illustrated in Figure 4. It can be seen the AAO structure is a close-packed hexagonal array of parallel cylindrical nanopores perpendicular to the surface on top of the underlying Al substrates. The parameters of the self-ordered AAO vary 10-400 nm for pore diameter, 50-60 nm for interpore distance and a pore density from 10^9 to 10^{11} cm [55,57]

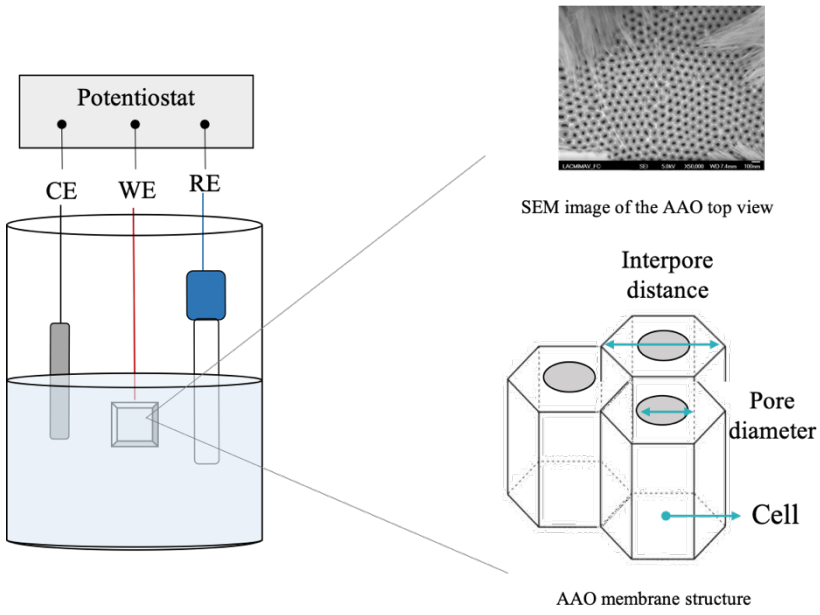

Figure 4. Electrochemical cell setup and AAO membrane structure.

This section includes some definitions for concepts used in the terminology for electrochemical measurements:

a) Capacitive current (density): is the current (density) flowing through an electrochemical cell that is charging/discharging electrical double layer capacitance and do not involve any chemical reactions (charge transfer). It is also called non-faradic or double-layer current.

b) Current: the movement of electrical charges in a conductor; carried by electrons in an electronic conductor and by ions in an ionic conductor. Two kinds of currents must be distinguished: direct current (DC) and alternating current (AC). The measurement unit of current is the ampere (1 A= $\frac{C}{s}$).

c) Direct current (DC): it is the unidirectional continuous flow of current.

d) Alternating current (AC): electric current which periodically reverses direction.

e) Electrical double layer: The structure of charge accumulation and charge separation that always occurs at the electrode-electrolyte interface. When the surface is charged is compensated with counter charges in the solution near the charged surface. The amount of charge is a function of the electrode potential and this structure behaves essentially as a capacitor.

f) Electrical potential: The electrical potential difference between two point in a circuit is the cause of the flow of a current. The measurement unit of the potential is the Volt (V).

g) Equivalent circuit: An electrical circuit comprised of series and parallel coupled resistors and capacitors and other elements that models the fundamental properties and behavior of electrodes or electrochemical cells.

h) Faradic current (density): The current (density) that is flowing through an electrochemical cell and is causing (or is caused by) chemical reactions (charge transfer) occurring at the electrode surfaces.

i) Open-circuit potential: The electrical potential of an electrode measured against a reference electrode when there is no current flowing through the electrode.

2.6. Background

This section includes a review on the state of art of three topics. First, the development and performance of FeS_2 nanoparticles embedded on inorganic or polymeric materials. Second, it is explained the core/shell nanostructures approach. Finally, the recent progress of Fe-based ternary chalcogenides for solar energy applications.

2.6.2 FeS_2-based solar cells

As noted above, FeS_2 in its cubic crystal structure owns desired optoelectronic and structural properties as photoactive material. However, FeS_2 has exhibited a poor performance once it is introduced in the photoactive layer in different kinds of solar cells. Table 1 compiles an overview of some works with FeS_2 as photoactive material. In 1986, Ennaoui *et al.* reported a solar cell with efficiency of 2.8%. Since then, many efforts have been done in order to develop iron pyrite solar cells with high efficiency. Although the challenges during the synthesis of pure FeS_2 made difficult this approach [58]. Ennaoui *et al.* work has become the base for the synthesis of FeS_2 although some characteristics and properties are still unclear and made difficult the understanding of the behavior of iron pyrite once it is incorporated in the photoactive material.

Table 1. Works reported for photovoltaic devices of FeS_2.

Author	Year	Efficiency (%)	System	Reference
Ennaoui *et al.*	1986	2.8	FeS_2	[58]
Lin *et al.*	2009	0.16	FeS_2/ P3HT	[59]
Kirkeminde *et al.*	2012	1.1	FeS_2:CdS	[60]
Steinhagen *et al.*	2012	0	FeS_2/P3HT	[61]
Richardson *et al.*	2013	2.89	FeS_2/ P3HT:PCBM	[62]
Middya *et al.*	2014	0.064	FeS_2/MEHPPV	[63]
Khan *et al.*	2014	0.5	FeS_2:CdSe	[64]
Luo *et al.*	2015	3.0	FeS_2/P3HT:PCBM	[65]
Luan *et al.*	2017	3.0	FeS_2/P3HT:PCBM	[12]
Matus *et al.*	2019	0.83%	FeS_2/P3HT	[66]

An adequate strategy to increase the performance of FeS_2 solar cells is to use a nanocrystal/polymer solid system well-known as hybrid solar cells. HSC have a particular feature since both inorganic semiconductor and polymers act as sunlight absorbers and excitons generators. In the state of art, FeS_2/polymer solar systems have been investigated. These polymers include the popular P3HT and the composite P3HT: PCBM, where the extended absorption to the red light region is common. Although as in many other cases, authors refer some problems such as high dark leakage current, which leads to a small open circuit voltage due to the presence of impurities of FeS_2 and surface defects that affect the electron transport. In order to obtain high efficiency FeS_2 solar cells (higher than 3%) , author agree on the importance of the optoelectronic

properties, the concentration effect and the film thickness of photoactive layer [59,61,62,64,67]. In 2019, Matus reported the fabrication of hybrid solar cells with the composition of FTO/TiO_2/P3HT:FeS_2/C:Au in superstrate configuration. In this work is established an important correlation between FeS_2 nanoparticles concentration and the efficiency since highest efficiency of 0.83% is obtained with 1 wt/wt. %. Moreover, it is indicated the importance of the TiO_2 layer to increase the charge extraction since this metal oxide increase the synergy in the carrier collection and separation [66].

Additionally, some blending materials with CdS and CdSe have been studied. Cd-chalcogenide and FeS_2 solid solar cells formed a donor/acceptor phase that improved the charge separation and transport. However, as it is usual for chalcogenides sulfur defects played an important role on the poor performance of these solar systems. An important contribution is observed since the film roughness seems to influence the reduction of reflection of light. On the other hand, high FeS_2 concentration increases the presence of defects that causes a faster recombination affecting the solar cell performance [60,63,65].

Despite these recent works and a renewed interest on FeS_2 as photoactive material, non-high performance device has been made based on this material. Further investigation into the fundamental properties of FeS_2 and deployment in alternative device architectures are required to fully explore the potential of FeS_2 for its use in PV. Strategies as core/shell arrays, Fe-based ternary chalcogenides and their incorporation

into a conducting polymer are reviewed in order to generate hybrid systems that exhibit an enhancement on its optoelectronic properties and therefore, in its energy conversion efficiency.

2.6.3 Core/shell and multishell nanocrystals

Combining two or more materials can enhance the optoelectronic properties due to the surface modification. In this work, it is referred to the overgrowth of the surface of the core with a shell of a second semiconductor, resulting in a core/shell arrangement. The core/shell materials exhibit an increase of photochemical stability and quantum efficiency due to the confinement of the exciton.

There are only a few works describing the FeS_2 interactions with another inorganic material. In 2017, McGrath *et al.* purposed the surface passivation of FeS_2 nanocrystals using an inorganic shell layer to eliminate surface trap states using iron selenide due to its chemical compatibility. The core/shell nanocrystals showed an increase on the optical and electrical properties, and surface stability. Moreover, the surface passivation with iron selenide allowed to obtain a multifunctional material since the nanocrystals exhibited a magnetic response [68]. In the same year, Rhodes' research group published the synthesis of FeS_2-CoS_2 core/shell nanocubes. In this work, it is discussed the importance of having a similar lattice parameter in order to promote the

growth of the shell over the core of iron pyrite. As well, it is demonstrated that altering the synthetic conditions can tune the shell thickness [69].

Commonly, core/shell nanostructures correspond to nanoparticles systems but recently, alternative nanostructures as 1D architectures have become popular. In particular, for PV 1D core/shell arrays are an interesting choice. One-dimension (1D) core/shell nanoarray structures are optimal architectures for smooth charge transport. In such architectures, charge transport is direct and fast due to the 1D nature while charge separation is efficient and controllable because it takes place in the radial versus the axial direction, and the charge collection distance is easy to be tailored by tuning the shell thickness.

In 2014, Ghrib *et al.*, reported the synthesis and characterization of ZnO/ZnS core/shell nanowires. ZnO nanowires of approximately 3 μm length and 200 nm diameter were prepared and ZnS nanoparticles deposited in a second-step. Improvement on its optical, electrical conductivity and structural properties are observed after the incorporation of ZnS nanoparticles. Similar effect can be seen in the work by He *et al.* in 2016, where due to the incorporation of ZnO nanorods and CuO nanoparticles in one system, the material showed an extended optical absorption to the visible region and enhancement on its photocatalytic activity [70-71].

As previous work in the research group in 2017 is reported the synthesis and characterization of FeS_2/ZnO core/shell nanowires that exhibited optical absorption in the visible range, charge transport between both materials and a suitable band gap, 1.3 eV, for PV applications [72]. In 2018, Fan *et al.* reported the synthesis of $FeSe_2$@C core/shell nanorods for sodium ion batteries. Even if the purpose of the material is different, this work addressed the interaction between iron selenide and carbon nanostructures. It is demonstrated that the structures exhibited high conductivity and structural properties that influence the charge transfer into the $FeSe_2$ [73]. In the development of core/shell nanowires, it is observed the influence of the core on the optical absorption and at the same time the core influences the separation and carrier collection while the shell thickness influences carrier collection.

2.6.4 Core/shell solar cells

On the other hand, core/multishell nanowires is an emerging field of study for several applications. It involves two or more conformal shells are grown around a core of a different semiconductor material. These radial heterostructures are the evolution of simple core/shell nanowires, where the core is wrapped by one-single shell [74]. In the field of PV, Sun *et al.* in 2011, reported three-component core/shell nanowires of poly (3-hexylthiophene)/CdS/ZnO. The material was obtained by electrodeposition of CdS nanoparticles and P3HT onto ZnO nanotubes. The hybrid material showed and enhancement on the optical absorption in the visible region and presented an interface between n-type CdS and p-type P3HT improving the charge separation. Energy

conversion efficiency up to 1.28% was obtained [75]. In 2017, Parize *et al* reported solar cells of $ZnO/TiO_2/Sb_2S_3$ and P3HT as the hole transport material. The solar cells with this compositions exhibited photo-conversion efficiency of 2.3%, short circuit current density of 7.5 mA/cm^2 and a high open circuit-voltage of 656 mV [76].

The polymeric materials within the hybrid solar cells act as the hole transport material. Moreover, when the conductive polymers are grown in 1D arrays is possible to enhance charge-transport rate and increase surface area, important parameters for electronic devices. In 2007 Xiao *et al.,* reported two model mechanism for the growth of nanotube structures of conductive polymers as poly(3,4-ethylenedioxythiophene) (PEDOT), polypyrrole and P3HT through electrochemical method assisted by anodic aluminum oxide (AAO) templates. First mechanism is based on electrochemical active sites and second-one is based on diffusion and reaction kinetics, with both paths is deduced that experimental parameters as monomer concentration and potential leads to nanowires or nanotubes and give insight about the formation of 1D nanostructures for different conductive polymers [77]. Numerous works reported the use of P3HT nanowires coupled with semiconductors such as CdS, ZnO among others, concluding the hybrid systems showed broad light absorption, efficient charge transport, enhancement in the device performance and stability. Moreover, these works remarked the importance of a perfect interfacial contact between organic and inorganic nanostructures, resulting in the development of high-performance hybrid solar cells [78-79].

2.6.5 Summary

The literature review summarizes that FeS_2 (pyrite) exhibits promising optoelectronic properties, non-toxicity, earth-abundant and processable solution to produce large-area and low-cost solar cells. FeS_2-based solar cells are estimated to cost 0.00019 ¢/kW to produce electricity compared to 3.9 $/kW for Si. Besides, it is anticipated low cost devices due to the film thickness (0.1 μm) that it is ten times lower than for other semiconductors. However, efficiencies up to 3% have not been reported yet due to the presence of isomorphs, surface defects, etc.

In order to develop high performance devices, authors agree the surface passivation with inorganic and polymeric materials can reduce or eliminate the typical surface defects and even can cause multifunctionality of FeS_2 nanocrystals. The coupling with another material in core/shell arrays has the requirement to use high-band gap semiconductor as shell and compatibility of the lattice parameters. For this reason, ZnO is a good choice to use in the strategy to increase the performance of the hybrid solar cells. Moreover, the insertion of metal oxide layers effectively suppresses the leakage current and reduces the serial resistance of the device.

On the other hand, nanotubular conducting polymer extends the optical range of absorption, enhances charge-transport rate, increases the surface area and provides chemical stability. Particularly, P3HT contributes to the optical absorption in the

visible and near-infrared range, in the hole mobility (0.1 $cm^2V^{-1}s^{-1}$) and facilitates the processability in solution. Moreover, P3HT exhibits suitable mechanical properties to be used in flexible devices.

Additionally, the use of multishells in a 1D array provide quantum confinement that can tune the optical absorption range and enhance the charge separation. Addressing some parameters of the FeS_2-based solar cells, it is important to consider the film thickness and concentration of iron pyrite nanoparticles.

Bearing in mind the state of the art, FeS_2-based/poly(3-hexylthiophene) hybrid solar cells offer an entry to develop high performance solar devices.

Scientific contribution

Hybrid solar cells of pyrite-based/poly(3-hexylthiophene) core/shell nanowires.

Hypothesis

Hybrid solar cells of pyrite-based/poly(3-hexylthiophene) core/shell nanowires exhibit an energy conversion efficiency up to 3%.

General objective

To obtain and characterize hybrid solar cells of core/shell nanowires of pyrite-based/ poly(3-hexilthiophene).

Specific objectives

1. To synthesize poly(3-hexylthiophene) by electrochemical method.
2. To characterize P3HT by UV-vis, PL, FT-IR, FE-SEM and DTA-TGA.
3. To synthesize ZnO nanorods and nanotubes by electrochemical method.
4. To characterize ZnO nanostructures by UV-vis, PL, FT-IR, FE-SEM and TEM.
5. To synthesize FeS_2 nanoparticles using complexing agents by microwave heating method.
6. To characterize FeS_2 nanoparticles by XRD, UV-vis, PL, FT-IR, FE-SEM and TEM.
7. To obtain hybrid films of FeS_2/ZnO/P3HT on ITO glass slide.
8. To characterize hybrid material by UV-vis, PL, FT-IR, and FE-SEM.

Chapter III

Materials and method

3.1. Electrodeposition of P3HT nanotubes

Before the electrochemical experiments for poly(3-hexilthiophene) are performed, alumina membrane will be coated with a thin layer of gold (ca. 250-300 nm thick) by evaporation using a Denton Vacuum Desk V. Au is introduced inside the pores and forms annular electrodes at the bottom of the pores, which act as a working electrode.

The growth of poly(3-hexylthiophene) nanotubes was performed with an Autolab PGSTAT302N potentiostat/galvanostat connected to a conventional three-electrode cell. The electrochemical cell consisted in an AAO membrane (Whatman Anodisc 25, pore size= 200 nm) as working electrode, a Ag/AgCl electrode as reference electrode and a platinum rod as counter electrode. P3HT nanotubes were synthesized in a solution with a mixture of inert electrolyte of 0.1 M tetrabutylammonium hexafluorophosphate ($TBaPF_6$) in acetonitrile and 5 mM 3-hexylthiophene (3HT) by a chronoamperometric method for 100 s under constant potential of 2.0 V [80].

After the electrodeposition, the electrochemical bath with acetonitrile and $TBaPF_6$ is disposed in the container E organic according to the current storage system for hazardous waste in FCQ, UANL.

3.2. Electrodeposition of a wide band-gap semiconductor

ZnO nanostructures are grown on ITO glass slide in order to form a p-n heterojunction with FeS_2, and a donor-acceptor interface between the wide band-gap nanocrystal and the conducting polymer.

3.2.2 Synthesis of ZnO nanotubes

Electrodeposition of ZnO nanotubes was based on She *et al.* report [81]. Electrochemical synthesis was performed with an Autolab PGSTAT302N potentiostat/galvanostat. A standard three electrodes system comprised Pt rod and a Ag/AgCl electrode as the counter and reference electrodes, respectively. ITO-coated glas (2.5 x 1 cm and active area of 2 cm^2) was used as working electrode. Electrolyte consisted in an aqueous solution of 5 mM $Zn(NO_3)_2 \cdot 6H_2O$ and 0.1 M KCl and temperature was kept at 80 ºC, while pH was adjusted to 6. To initiate electrodeposition, stationary potential varied from -0.8 V to -1.0 V vs. Ag/AgCl. Growing process was studied for 600 s and 2000 s.

ZnO nanotubes were obtained using the synthesized ZnO nanorods in the first step. ZnO nanorods were immersed in 0.125 M KOH solution at 85 ºC for 20 minutes [82]. ZnO nanotubes are washed with deionized water and dry at room temperature.

The aqueous solution of the electrochemical bath with the rest of the mixture of $Zn(NO_3)_2 \cdot 6H_2O$/KCl and the KOH solution are disposed in the container A according to the current storage system for hazardous waste in FCQ, UANL.

3.3. Synthesis of FeS_2 by microwave heating method

The reaction was carried out as follows. In a vessel, 1 mmol of anhydrous iron chloride (II) and 4.5 mmol of sodium thiosulfate were mixed with 50 mL of ethylene glycol and kept under magnetic stirring for 15 minutes. Then, 4 mmol mercaptopropionic acid (MPA) were added to the solution under continuous stirring. Finally, 7 mL of deionized water was added. Microwave heating was performed on the reaction mixture in cycles of 10 s ON and 30 s OFF at 100% microwave power (1000 W, 2.45 GHz). Solutions reacted with a total heating time of 150 s or 210 s. Reaction finalized when grayish-black powder appears. The end product was centrifuged and washed several times with deionized water, ethanol and acetone. In order to purify the black powder was washed with hydrochloric acid 2 N. Finally, the product was dried under N_2 flux at room temperature for 15 minutes.

3.3.2 Stability study of pyrite nanoparticles and infiltration process

Pyrite was prepared in the same conditions as described before but adding a complex agent of sodium citrate or sodium tartrate in 1:4 molar ratio with Fe^{2+} source. Mixed

solution was heated for 300 s and 360 s. The black powder was centrifuged and washed with deionized water, ethanol and acetone. After the synthesis of FeS_2 nanoparticles, it is infiltrated within the P3HT/ZnO nanostructures through electrophoretic deposition. The deposition potential and time was 3 V for 2 h. The core/shell arrays inside the AAO membranes will be dried at 50 ºC for 1 h [72].

The disposal of the solvents used for the reaction mixture of FeS_2 and its purification are disposed in the container C. While the HCl is disposed in the A container according to the current storage system for hazardous waste in FCQ, UANL.

3.4. Fabrication of hybrid solar cells

3.4.2 Cleaning substrates

The main substrate for the fabrication of hybrid solar cells is ITO covered slide (20 Ω/sq). The glass slide is cut into 25 mm squares prior to cleaning process. The cleaning protocol is carried out as follows: firstly, samples are washed with deionized water and detergent. Then samples are sonicated sequentially in isopropyl alcohol and acetone for 15 minutes each. The slides are dried at room temperature with N_2.

3.4.2 Active layer deposition

The structure of the three combinations of the hybrid core/shell nanostructures is shown in Figure 5. It consists in a sandwich-type cell using ITO glass as photoanode, the photoactive layer of the hybrid core/shell nanowires and Au coat as cathode. The active layer, consisting of the one-dimensional hybrid core/shell nanostructures (FeS_2/ZnO/P3HT) is deposited onto ITO glass slide (200 nm to 300 nm) using electrochemical method. The temperature of the active layer during characterization is room temperature.

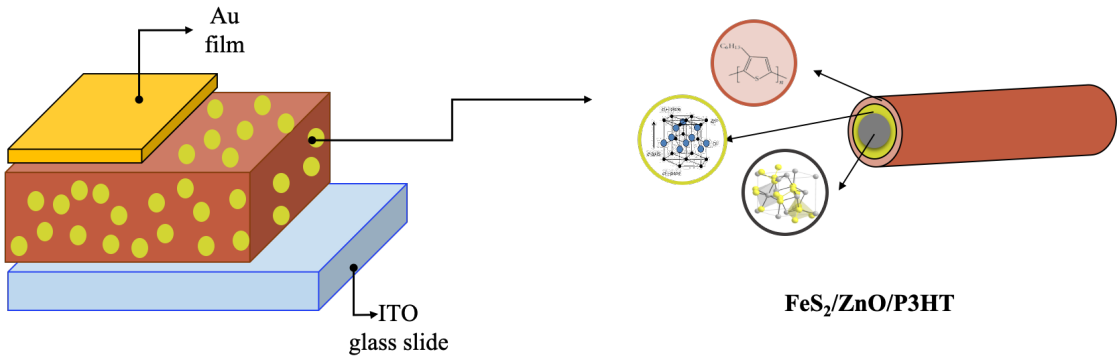

Figure 5. Architecture of the hybrid solar cells purposed in this work.

3.5. Characterization techniques

UV-visible spectroscopy (UV-vis): involves the spectroscopy of photons in UV-visible region. This region includes wavelength from 10 to 780 nm and the limit between both of them is around 390 nm. UV-visible radiation originates due to the rearrangement of outer and inner electrons. The process involved in the interaction of matter and

radiation are transmission, absorption and reflection.

The inorganic, polymeric semiconductors and hybrid material absorption spectrum and band gap estimation are characterized using a spectrophotometer Shimadzu UV-1800 (Laboratorio de Materiales I, FCQ, UANL). Band gap estimation is estimated by the following equations:

$$Eg = \frac{hc}{\lambda} \quad (2)$$

where, h is Planck's constant (6.626×10^{-34} J·s), c is the speed of light (3.0×10^{8} m/s) and λ is the cut off wavelength.

It is considered a second method for band gap estimation by the Tauc's plot:

$$(\alpha h\upsilon)^2 = k(h\upsilon - Eg) \quad (3)$$

where, α is the absorption coefficient, k is a proportionality constant, h is the Planck's constant, υ is the frequency of the incident beam and Eg is the optical band gap.

The absorption coefficient (α) is determined by:

$$\alpha = \frac{1}{d}\ln(A) \quad (3)$$

where, d is the thickness of the film and A is the absorption.

Photoluminescence spectroscopy (PL): involves two process, (1) the absorption of

energy from a light source and the subsequent (2) emission of light. It includes the radioluminescence, electroluminescence, chemiluminescence, photoluminescence and bioluminescence depending of the energy source. Information as the presence of impurities and its dependence on the level of photo-excitation is related to the recombination process and can be revealed by the emission spectrum. Moreover, PL is very sensitive to surface effects or adsorbed species of semiconductor particles allowing the study of electron-hole surface process.

Typical transitions and quenching fluorescence are studied by collecting the emission spectra at room temperature of inorganic semiconductors, conducting polymer and hybrid materials using a fluorescence spectrometer Perkin Elmer LS55 (Laboratorio de Materiales I, FCQ, UANL)

Fourier-transform infrared spectroscopy (FT-IR): is a technique based on the vibrations of the atoms of a molecule. The infrared spectrum can be divided into three main regions: the far-infrared (<400 cm^{-1}), the mid-infrared (4000–400 cm^{-1}) and the near-infrared (13000–-4000 cm^{-1}). FT-IR spectrum covers the interpretation of the vibrations as bands that appear which, are assigned to a particular bonding of a molecule, known as group frequencies. This information allows a partial recognition of the target molecule supporting information is needed in order to elucidate a molecule.

It elucidates the presence of organic and/or other compounds in the inorganic films, to characterize the vibration modes of poly(3-hexylthiophene) and composites. FT-IR spectrum is recorded using a Perkin Elmer Spectrum Two in the range of 500-4000 cm^{-1} at room temperature in reflectance mode (Laboratorio de Materiales I, FCQ, UANL).

X-Ray Diffraction (XRD): refers to the electromagnetic radiations with wavelength of 10^{-3} nm to 10 nm. X-ray diffraction is essentially a scattering phenomenon in which a large number of atoms are involved. Since the atoms in a crystal are periodically arranged, the X-rays scattered by these atoms can be in phase and constructively interfere in a few directions

Crystalline phase and crystallite size estimation using Debye-Scherrer equation are determined on a Brucker D2 Phaser with a CuKα radiation (Kα= 1.54056 Å). Data are collected by scanning from 5° to 90°. (Laboratorio de Materiales II, FCQ, UANL).

$$D = \frac{0.9\lambda}{\beta cos\theta} \quad (4)$$

where, D is the diameter of crystallites, λ is the wavelength of the X-ray source, β is the full width at half of its intensity in radians and θ is the Bragg's angle.

Potentiostat/Galvanostat: electrochemical measurements are performed using an Autolab PGSTAT302N.

a) Cyclic Voltammetry: to determine growth mechanism of inorganic semiconductors and conducting polymer. Moreover, HOMO and LUMO positions will be determined by the onset potentials of oxidation and reduction in order to evaluate the Eg value for inorganic materials, polymer and composites.

$$E(HOMO) = -[E_{ox}^{onset} + 4.4]\ eV \quad (5)$$

$$E(LUMO) = -[E_{red}^{onset} + 4.4]\ eV \quad (6)$$

$$\Delta E = E(LUMO) - E(HOMO) \quad (7)$$

b) Chronoamperometry: is used to study the kinetics of chemical reactions, diffusion process, and adsorption. It consists to held a constant potential of the working electrode at which the redox reaction occurs monitoring the resulting current as a function of time. Reactions under diffusion control follows the Cottrell equation:

$$i = \frac{nFAc_j^0\sqrt{D_j}}{\sqrt{\pi t}} \quad (8)$$

where, i is the current (A), n is the number of electrons (to reduce/oxidize one molecule of analyte), F is the Faraday constant (96,485 C/mol), A is the area of the electrode (cm^2), c_j^0 is the initial concentration of the reducible analyte (mol/cm^3), D_j is the diffusion coefficient for species (cm^2/s) and t is time (s).

To determine parameters as time and applied potential to grow the nanorods and nanotubes of inorganic semiconductors and polymeric matrix.

c) Electrochemical Impedance spectroscopy (EIS): is a useful tool to study the charge transfer and transport. It is based on the application a sinusoidal perturbation AC voltage (or current) to the studied material response as a function of frequency.

To estimate conductivity of polymer and composites thin films through the Bode and Nyquist plots.

$$\sigma = \frac{L}{RA} \tag{9}$$

where, L is the thickness of the film, R is the impedance resistance of the model circuit and A is the area.

Field Emission Scanning Electron Microscopy (FE-SEM): uses an electron beam of high-energy electrons to generate a variety of signals at the surface of solid samples. Areas ranging from approximately 1 cm to 5 microns in width can be imaged in a scanning mode using conventional SEM techniques (magnification ranging from 20 X to approximately 30,000 X, spatial resolution of 50 to 100 nm). The SEM is used to generate high-resolution images of shapes of objects (SEI) and to show spatial variations in chemical compositions (1) acquiring elemental maps or spot chemical analyses using EDS, (2) discrimination of phases based on mean atomic number

(commonly related to relative density) using Backscattered electron images (BSE), and (3) compositional maps based on differences in trace element using cathodoluminescence (CL).

The morphology and size distribution of inorganic semiconductors and conducting polymer is given by a field emission scanning electron microscope, JEOL JSM6701F. (Laboratorio de Microscopía, FCQ, UANL).

Chapter IV

Results and discussion

4.1. Electrodeposition of poly(3-hexylthiophene) nanotubes

4.1.2 Synthesis conditions and reaction mechanism of P3HT.

The cyclic voltammogram for 3-hexylthiophene (3HT) and $TBaPF_6$ in acetonitrile solution obtained at 0.1 V/s is shown in Figure 6. Voltammogram shows typical electrochemical behavior of P3HT. Two distinct oxidation potentials were found. The first oxidation peak was measured at +0.78 V (partially p-doped state) and the second oxidation peak was found at +1.3 V (highly p-doped state), where the maximum current is observed. This current is indicative that most of the monomer units are oxidized [83, 84]. On the other hand, reduction peak was measured at a more positive potential of +0.4 V. A third state where the polymer is predominantly in its undoped or neutral state is found at low potentials (<0.3V) [85]. Therefore, the window potential for the polymerization of 3HT is established from +1.3 V to +2.5 V.

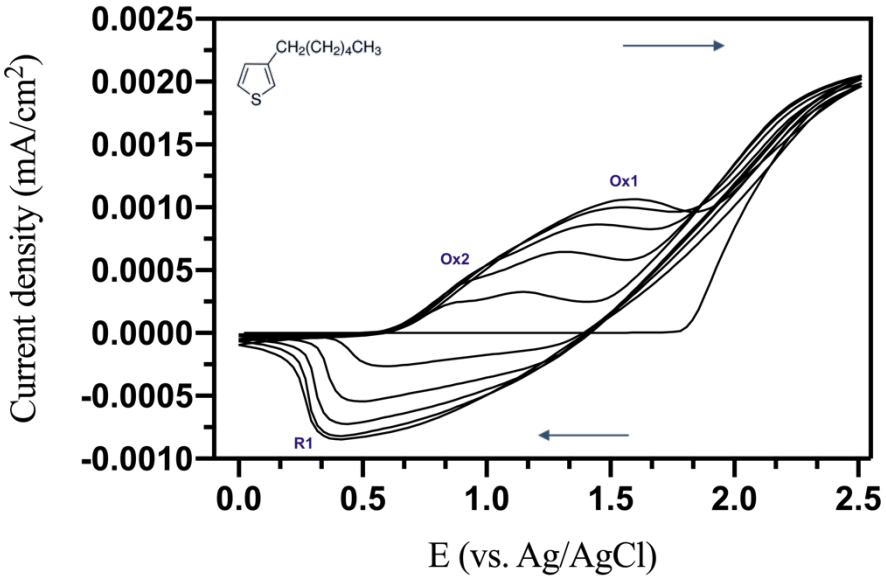

Figure 6. Cyclic voltammetry of P3HT electrodeposited on ITO in 0.1 M $TBaPF_6$ recorded at room temperature. Scan rate 0.1 V/s.

Figure 7 shows the current-time transients for the deposition of P3HT at different times with a constant potential of +1.9 V. Initial high current density is associated to the charging of double layer of the electrode (capacitive current) and is followed by faradic current with the oxidation of 3HT, where is formed a plateau that keeps constant with the increasing time. Thus, it can be inferred the only process that takes place is the growing of the monomer chains. Mechanism of P3HT electropolymerization (Figure 8) describes that in a first step are formed oligomer chains in the solution near to the ITO surface due to the oxidation process. Second step corresponds to the nucleation of the oligomer chains that reach a molecular weight to precipitate on the electrode surface [86,87]. Therefore, it is expected that this current-time dependence influence the current density generated by the applied potential [88].

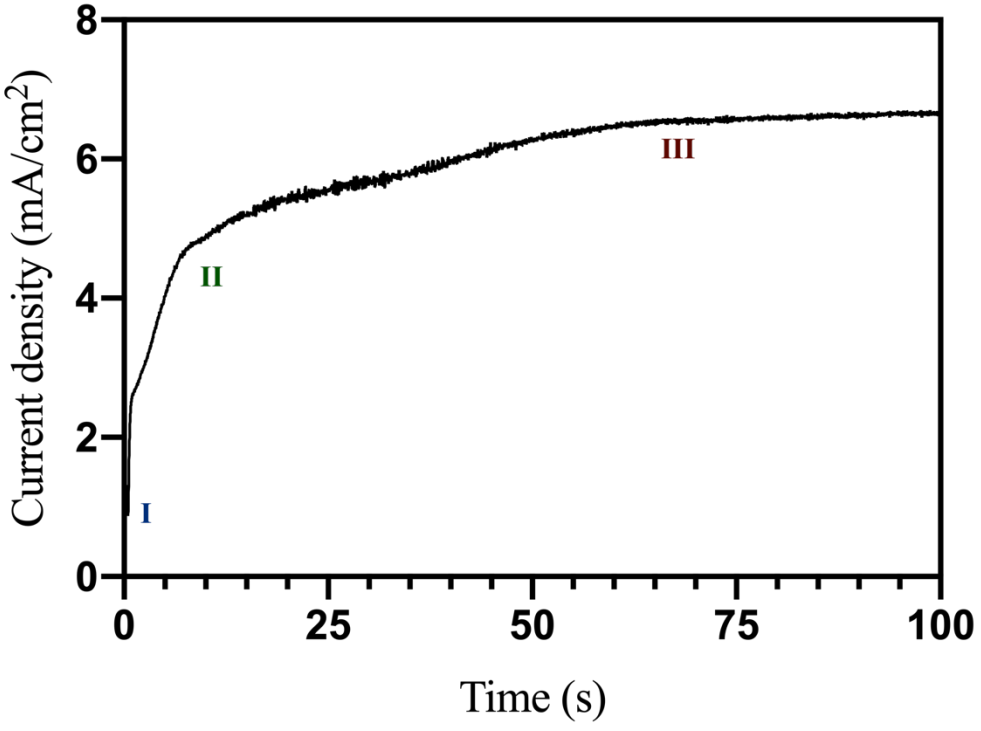

Figure 7. Chronoamperometric curve of P3HT electrodeposited on ITO at room temperature.

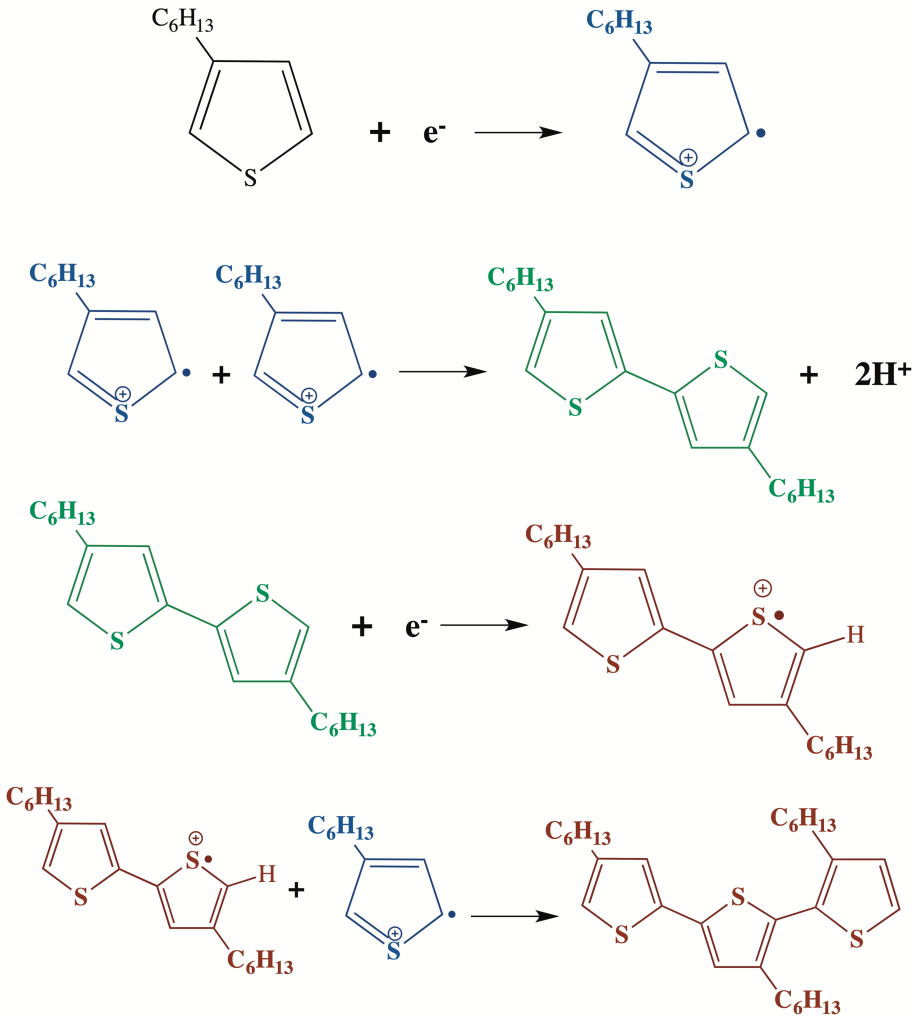

Figure 8. The reaction mechanism of the 3-hexylthiophene electropolymerization

4.1.3 Characterization of P3HT

Figure 9 shows the main characteristic bands of P3HT by FTIR analysis. The spectrum showed the vibrational bands of P3HT located at 3054 cm^{-1} corresponding to aromatic C-H stretching vibration of the thiophene ring. Stretching C-H aliphatic (CH_2 out of the phase, symmetric -CH_2 moieties vibrations and -CH_3 asymmetric vibrations on the

thiophene ring) are located to 2955 cm^{-1}, 2925 cm^{-1} and 2855 cm^{-1} [89, 90]. More vibrational bands are located at 1450 cm^{-1} (bending vibration bond of C-H), 1290 cm^{-1} (C-C symmetric stretching mode) and 725 cm^{-1} (band associated with CH_3 rocking vibration). The bands at 1118 cm^{-1} and 821 cm^{-1} are associated to the C-S stretching mode and the aromatic C-H out of plane vibration of the ring [91]. These functional groups are consistent with the chemical structure of P3HT and the applied potential does not modify them. Additionally, the intense vibration of the C-H out of plane deformation mode is associated with the stacking structure of conjugated rings since this vibration mode is attached to the conjugated ring and its vibration influence the π-π stacking [92].

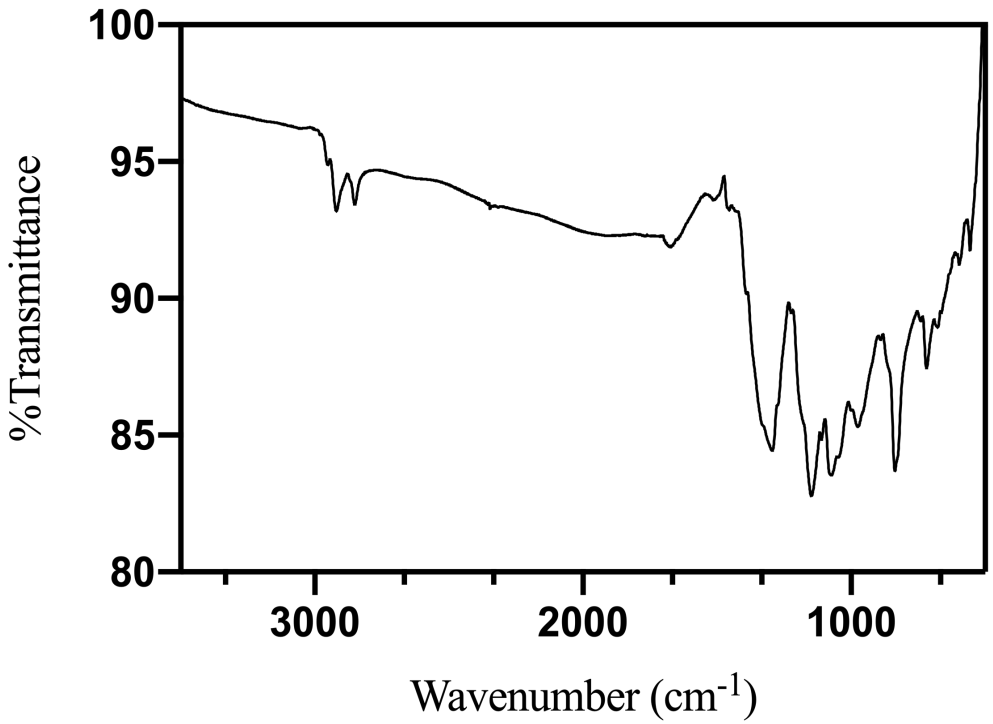

Figure 9. FT-IR spectrum of the poly(3-hexylthiophene) thin film.

The optical absorption spectra of P3HT film deposited on ITO in the wavelength between 350 nm to 1100 nm, is shown in Figure 10. The UV-vis spectrum of the P3HT film showed two broad absorption peaks at 520 nm (Eg_{op}= 2.38 eV) and 820 nm (Eg_{op}= 1.51 eV). These bands are associated to the $\pi \rightarrow \pi^*$ transition attributed to the crystalline π-π stacking structure of polymer P3HT chains. (charge transfer mechanism in regioregular P3HT) [93]. As higher the π-π stacking is, more pronounced and intense are these vibrionic peaks [94], which infers a better quality of the P3HT obtained resulting in a material with absorption properties associated to the dope state of the P3HT.

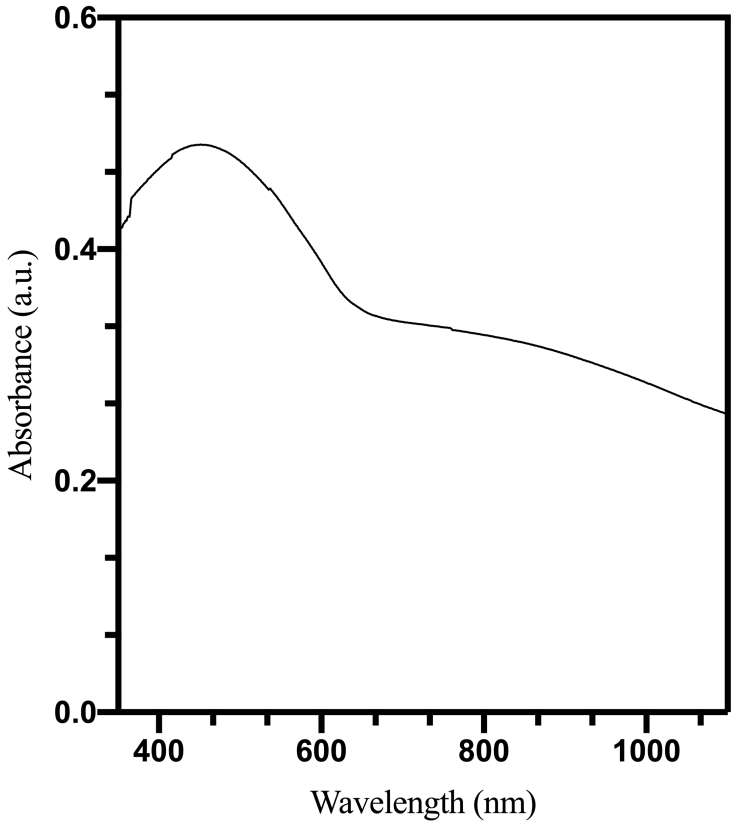

Figure 10. Optical absorption of poly(3-hexylthiophene) thin film.

4.1.4 Overview: Poly(3-hexylthiophene)

The P3HT obtained shows feasible optical and structural properties for flexible and light-weighted hybrid solar cells. In summary, P3HT exhibits a broad absorption in the optical spectrum indicative of the p-doping of the donor material while the cathodic deposition allows to obtain a consistent chemical structure with vibrations that influence the π-π interactions along the polymer backbone. These interactions are highly related to a high hole mobility of the P3HT. All these properties mean an important advantage for the hybrid solar cells. Moreover, the coupling between this polymer and the inorganic nanocrystals allows to enlarge the optical absorption and the stable structure of the P3HT keeps the conducting properties all along the backbone and therefore, efficient transport between the donor-acceptor interface.

4.2. Electrodeposition of ZnO nanostructures

ZnO (type n) is the semiconductor of interest to obtain a pn junction with FeS_2 (type p), the following experiments correspond to the synthesis of ZnO by electrochemical method. It was reproduced the experimental conditions for She *et al*. report [80]. Electrochemical deposition of zinc oxide initiates by the reduction of nitrate to form nitrite ions that produces hydroxide ions and causes the precipitation of $Zn(OH)_2$ onto the cathode. Finally, $Zn(OH)_2$ dehydrated to form ZnO due to temperature effect. ZnO deposition can be summarized by the following chemical equations [95,96]:

$$NO_3^- + H_2O + 2e^- \rightarrow NO_2^- + 2OH^- \quad (10)$$

$$Zn^{2+} + 2OH^- \rightarrow Zn(OH)_2 \quad (11)$$

$$Zn(OH)_2 \rightarrow ZnO + H_2O \quad (12)$$

Global reaction:

$$NO_3^- + Zn^{2+} + 2e^- \rightarrow NO_2^- + ZnO \quad (13)$$

Cyclic voltammetry was performed in solutions with 5 mM $Zn(NO_3)_2$ and 0.1 M KCl. A typical voltammogram for Zn deposition/dissolution process is given in Figure 11. It can be distinguished three zones. First zone corresponds to Zn^{2+} reduction into Zn metallic (below -1.0 V). Second zone (at -1.0 V to -0.8 V) is where the reduction of nitrate ions takes place. Finally, third zone corresponds to the disappearance of anodic peak due to zinc dissolution [97]. Since the ZnO deposition is governed by the nitrate ions reduction is established a window potential from -1.0 V to -0.8V.

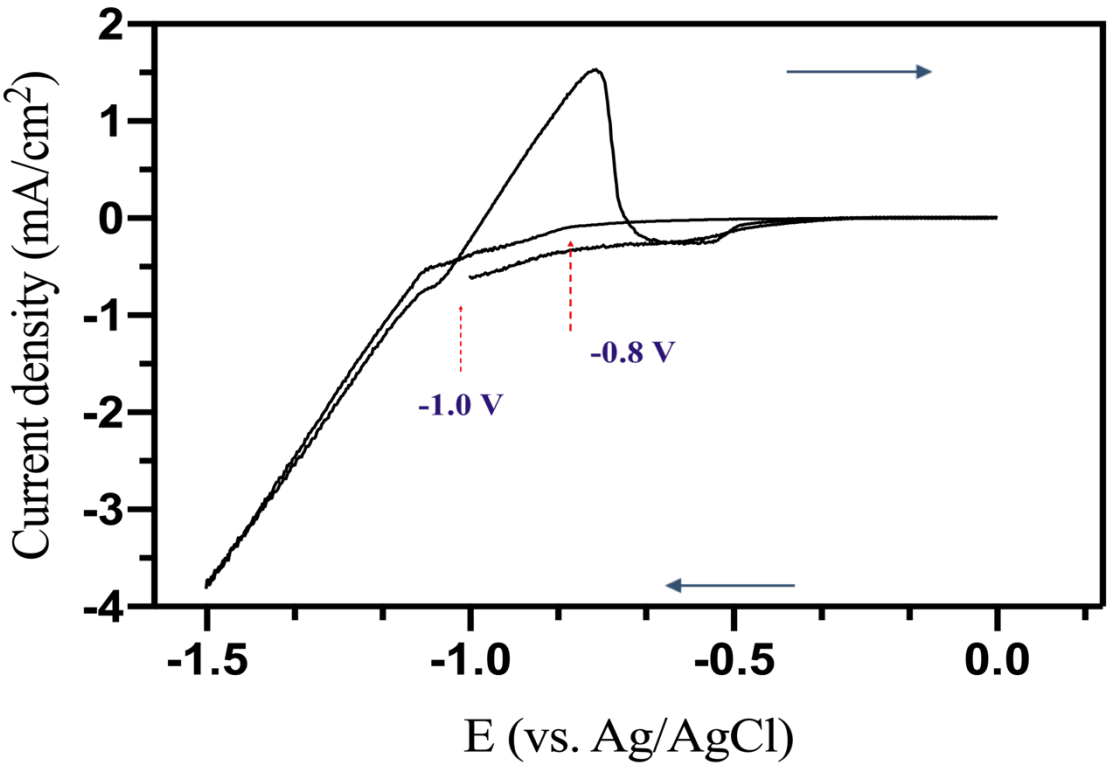

Figure 11. Figure 11. Cyclic voltammetry of ZnO electrodeposited on ITO glass at 70 ºC. Scan rate 0.05 V/s.

The kinetics of the ZnO deposited onto ITO was studied by chronoamperometric curves. Chronoamperometric curves in Figure 12 (a) and (b) for ZnO deposited on ITO at -1.0 V and -0.8 V at 70 ºC. Both curves show typical behavior for nucleation and growth. In the first step at short times corresponds to nucleation process on the active sites of ITO glass. As the pH increase $Zn(OH)_2$ is formed and transformed fully or partially, into ZnO film due to temperature effect (second step) [95,98,99]. The growing process of ZnO is described in the following chemical equations:

$$Zn^{2+} + \frac{1}{2}O_2 \rightarrow 2e^- + ZnO \quad (14)$$

$$Zn^{2+} + H_2O + \frac{1}{2}O_2 \rightarrow 2e^- + Zn(OH)_2 \quad (15)$$

The ZnO thin film morphology and orientation showed a correlation with current density-time curves. Thus, ZnO deposition could be increased and morphology could be influence by (1) cathodic current density and (2) the number of nucleation sites [100]. Cathodic current corresponds to the reduction of O_2 and NO_3 ions; therefore, as increase the cathodic current density, increases the local pH at the electrode surface, which leads to increase ZnO deposition due to higher nucleation sites. Comparing curves of E= -1.0 V and E= -0.8 V experiments, the effect of current density can be seen clearly since as higher the stationary potential is (-0.8 V) higher is the current density generated causing faster reactions and more mass deposited on the electrode surface.

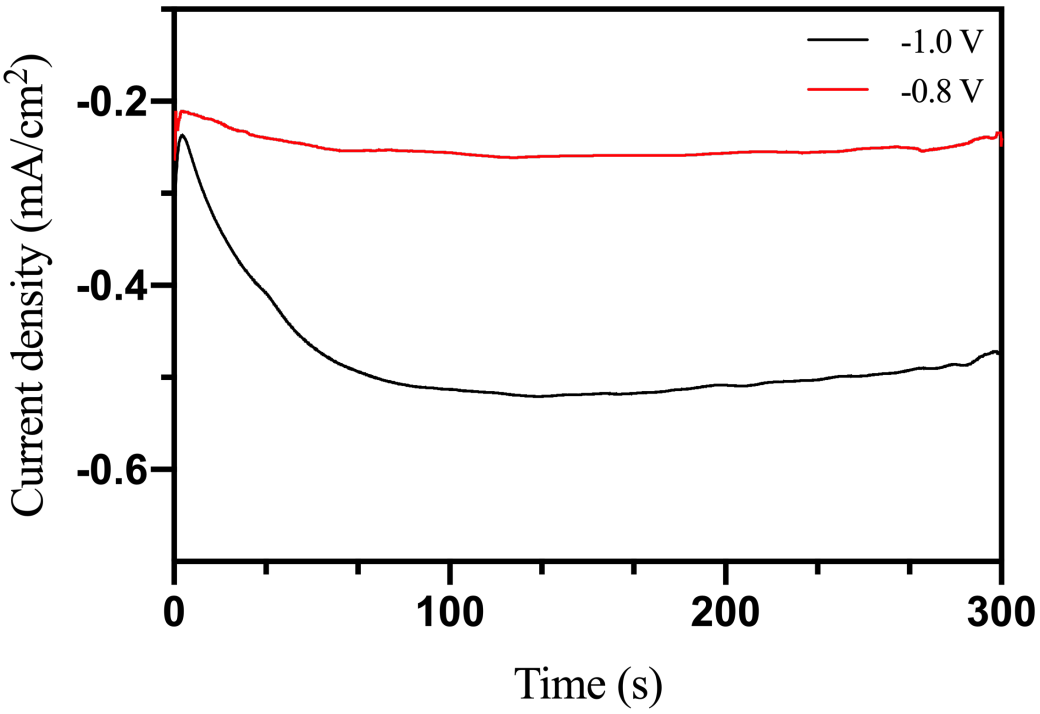

Figure 12. Chronoamperometric curve of ZnO electrodeposited on ITO glass at 70 ºC. potential of (a) -1.0 V and (b) -0.8 V.

The UV-vis spectra of electrodeposited ZnO at 70 ºC for E= -1.0 V and E= -0.8 V samples are shown in Figure 13 (a) and (b). Typical excitonic absorption at about 370 nm, it corresponds to the direct band gap of ZnO, 3.35 eV, and a second absorption peak around 440 nm, which is characteristic for ZnO nanorods and its attributed to the strong exciton effect due to the quantum confinement that present 1D nanostructures [101-103]. Quantum confinement theory describes the electrons and holes in the conduction and valence band, respectively are confined spatially by the potential barrier of surface and due to their confinement the optical transition energy from valence top to conduction bottom increases and the absorption maximum shifts to the

shorter wavelength region [105]. In the case of nanorods, the optical absorbance of ZnO nanorods increased rapidly after the energy of the incident photons became higher than the band gap. This is an indicator that the ZnO semiconductor absorbs the light at the edge of the visible region. Working at the edge of the visible region gives high stability and less noise to devices based on the ZnO nanostructure [101].

As described in the discussion of chronoamperometric curves, ZnO nanorods growth are strongly influenced by the current density generated; however, comparing (a) and (b) spectrum for the experiments E= -1.0 V the nanorods tend to grow faster than for E= -0.8 V samples, which can be attributed to the potential applied since -0.8 V corresponds to $Zn(OH)_2$ generation potential, where partially ZnO formation could be affecting the optical properties.

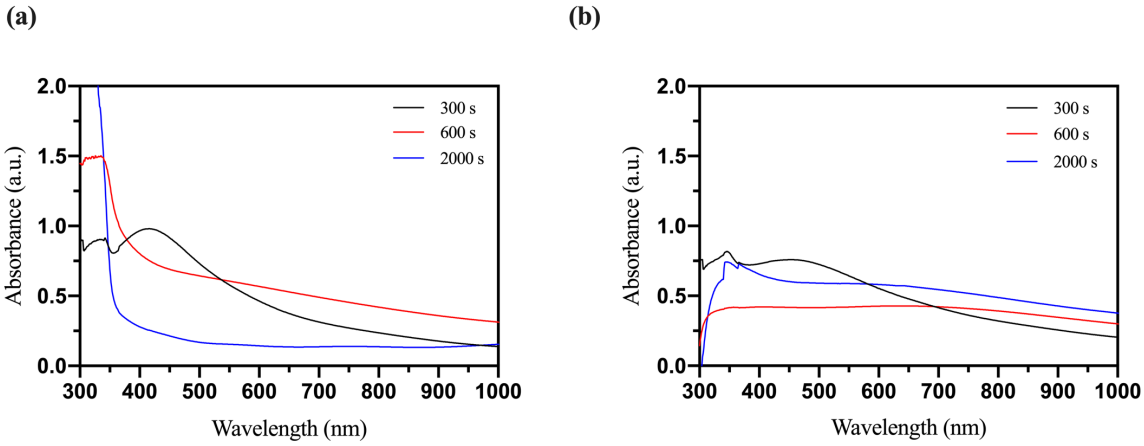

Figure 13. UV-vis spectra of ZnO electrodeposited at 70 ºC with applied potential of (a) -1.0 V and (b) -0.8 V.

Figure 14 shows the ZnO emission spectra at room temperature at different synthetic conditions using an excitation wavelength of 380 nm at room temperature. It is found two weak emissions at 420 nm and 480 nm while at 540 nm is observed a strong emission. The emission peak at 420 nm corresponds to UV emission attributed to excitonic recombination of the near-band edge emission. It has been reported the band- edge emission shifting in ZnO nanostructures with different concentrations of native defects. The weak emission at 480 nm is attributed to exciton transitions and various point defects. A strong green emission is observed at 540 nm [104-106]. The origin is attributed to the singly ionized oxygen vacancy (Vo) in ZnO and its recombination with a photogenerated hole. These deep-level emissions are related to a radiative transition from donors {Zinc interstitial (Zni), Oxygen vacancy (Vo)} to acceptors {Zinc vacancy (Vzn), oxygen interstitial (Oi)} [106-108]. The literature reports that nanorods exhibit more surfaces for oxygen vacancies due to their large aspect ratio [109, 110], therefore the difference of the emission intensity can be related to the different diameter and length obtained in the two different conditions.

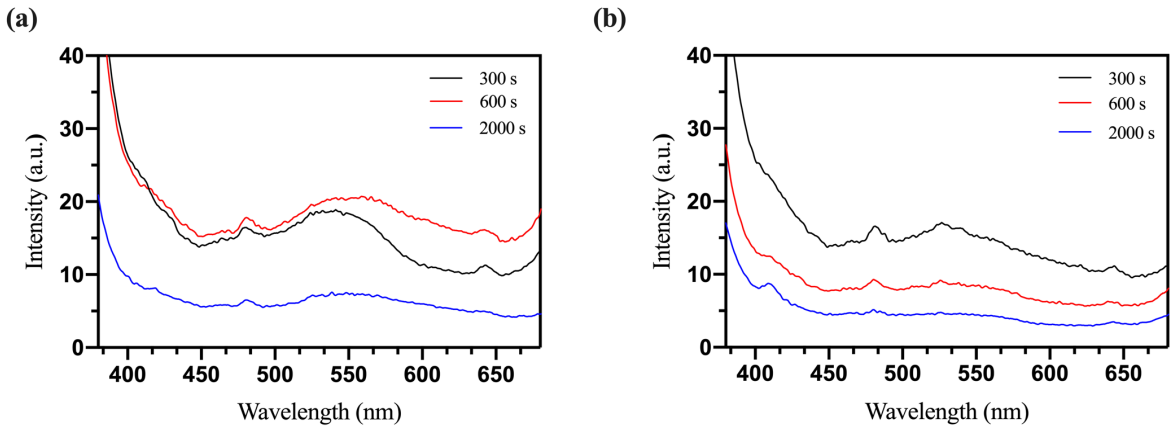

Figure 14. Emission spectra of ZnO electrodeposited at 70 ºC with applied potential of (a) -1.0 V and (b) -0.8 V.

4.2.2 Effect of temperature in ZnO electrodeposition

The cyclic voltammograms at 80°C on a ITO-coated glass electrode in 0.1M KCl were recorded between -1.5 V and 0 V is shown in Figure 15 and compared with Figure 11, same electrochemical growing process described the deposition of ZnO on ITO glass although $Zn(OH)_2$ reaction and ZnO formation potential shifted to -0.7 V and -1.1 V, respectively. Shifting can be attributed as effect of temperature and for better explanation about its influence is described with chronoamperometric curves.

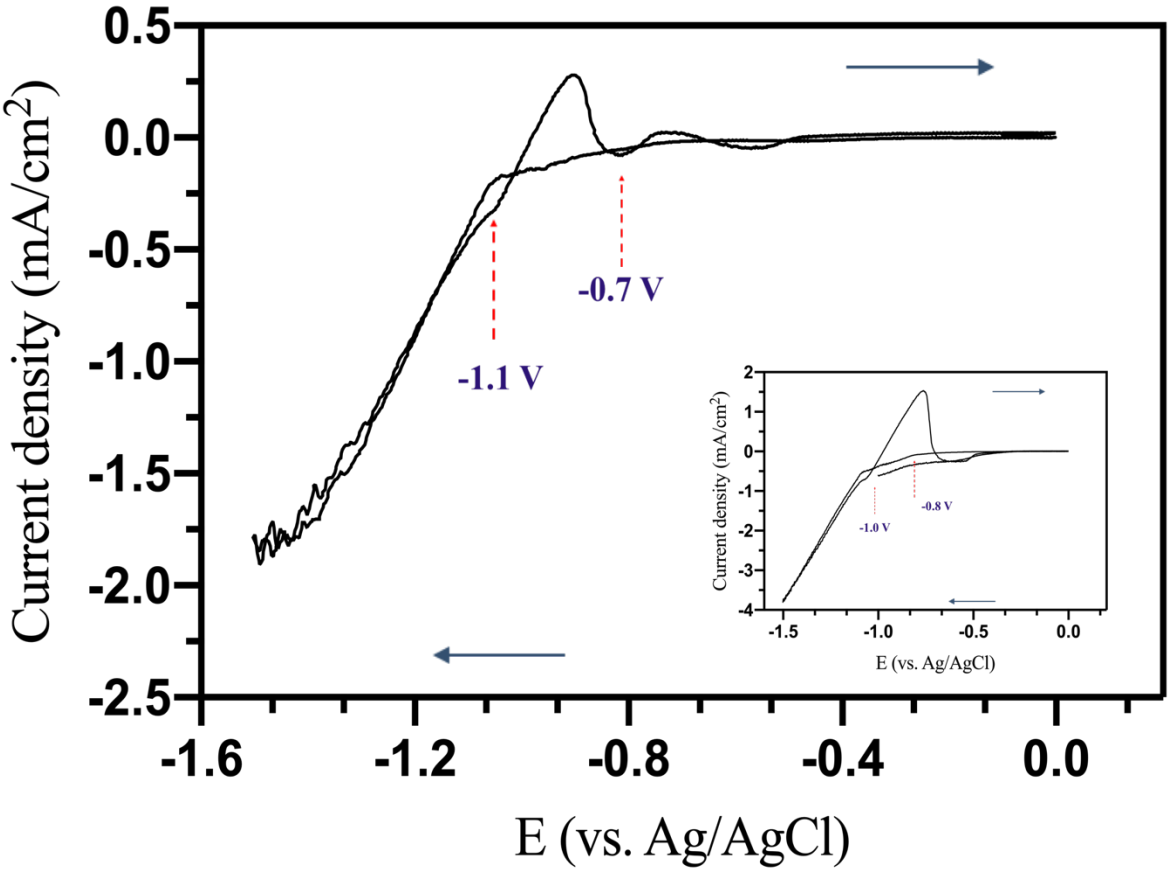

Figure 15. Cyclic voltammetry of ZnO electrodeposited on ITO glass at 80 ºC. Scan rate 0.05 V/s.

Chronoamperometric curves for ZnO at stationary potential -1.0 V and -0.8 V and temperature of 80 ºC are shown in Figure 16 described as expected the nucleation and growing process for ZnO nanorods and in a good agreement with the effect of temperature (80 ºC). According literature crystallization of ZnO started at 34 ºC, where nucleation is a delayed process and appears after induction period. As the temperature increases, two important phenomena are observed: (1) nucleation-growth peak becomes more intense and narrower and (2) induction period decreases and becomes very short at 60 ºC [111]. Thus, the temperature influences the electrochemical reaction kinetics, which explain the difference between the experiments at 70 ºC and 80 ºC.

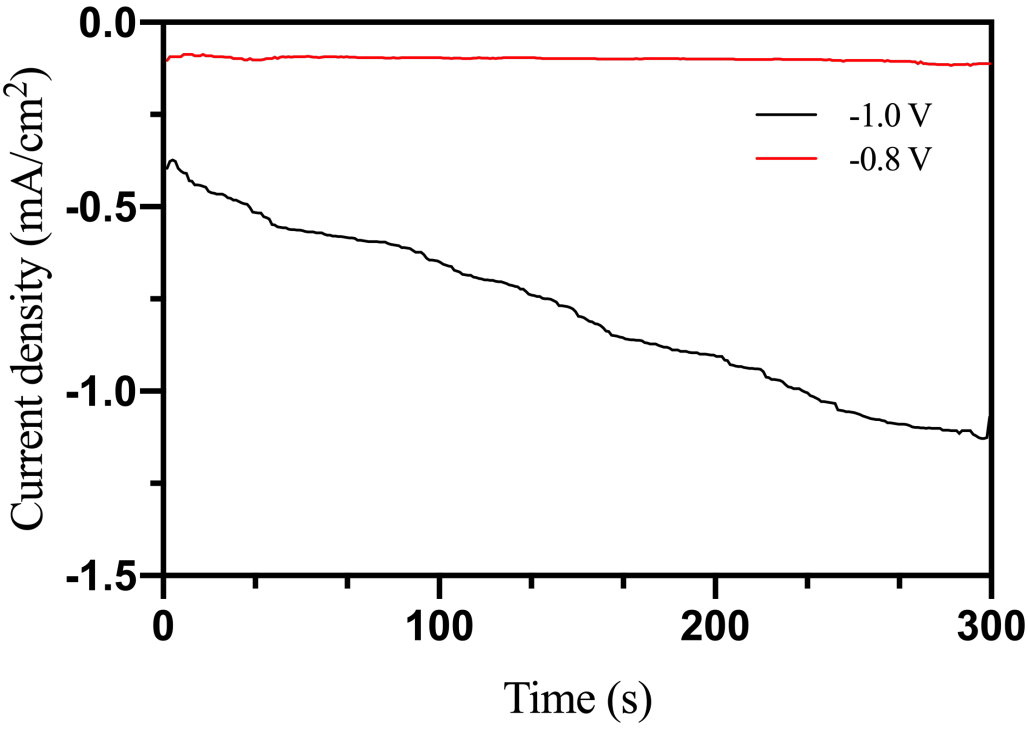

Figure 16. Chronoamperometric curve of ZnO electrodeposited on ITO glass at 80 ºC.

UV-vis spectra for ZnO electrodeposited in conditions of -1.0 V and -0.8 V at 80 ºC from 200 nm to 1100 nm are shown in Figure 17 (a) and (b). Samples 300 s and 600 s showed typical absorptions for nanorods at 350 nm, and from 500 to 550 nm in Figure 17 (a). However, sample t= 2000 s showed typical behavior for thin films or another ZnO nanostructures with excitonic absorption at about 350 nm. In addition, t= 300 s sample compared with t= 600 s showed a lower absorption intensity attributed to the amount and quality of nanorods obtained since its quantum confinement influences the absorption shifting to visible wavelength region. While in Figure 17 (b) absorption intensity is lower for samples obtained at E= -0.8 V due to the correlation between the stationary potential and the current generated that influences the growth all along the substrate.

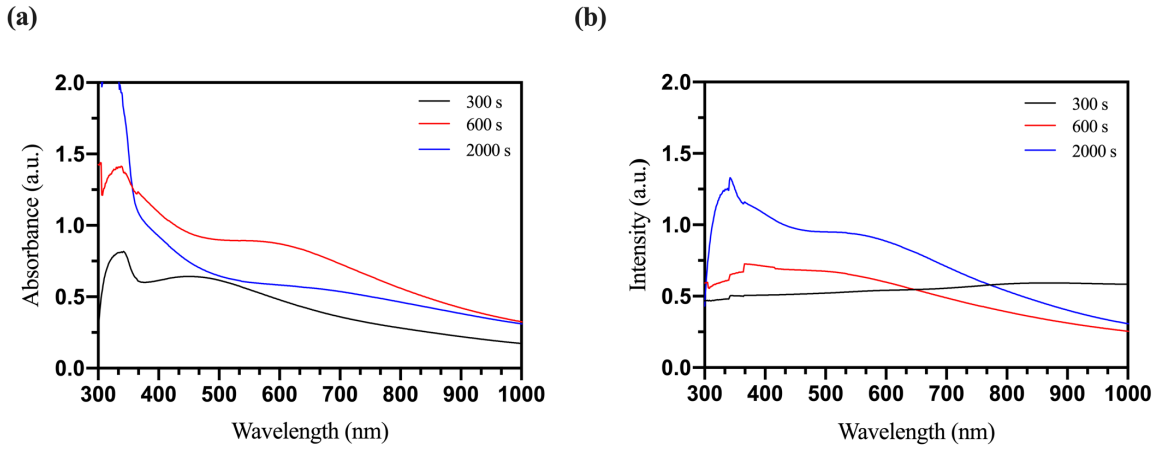

Figure 17. UV-vis spectra of ZnO electrodeposited at 80 ºC with applied potential of (a) -1.0 V and (b) -0.8 V.

Emission spectra of ZnO electrodeposited in conditions of E= -1.0 V and E= -0.8 V at 80 ºC from 380 nm to 680 nm are shown in Figure 18 (a) and (b). Same optical behavior

is observed for all the samples in both conditions (-1.0 V and -0.8 V), UV emission and green emission at about 480 nm and 525 nm, respectively. In addition, it is observed a significant difference in intensity between samples 600 s at -1.0 V and 2000 s at -0.8 V attributed to the quality of the nanorods (crystallinity) obtained and the low level of O vacancies.

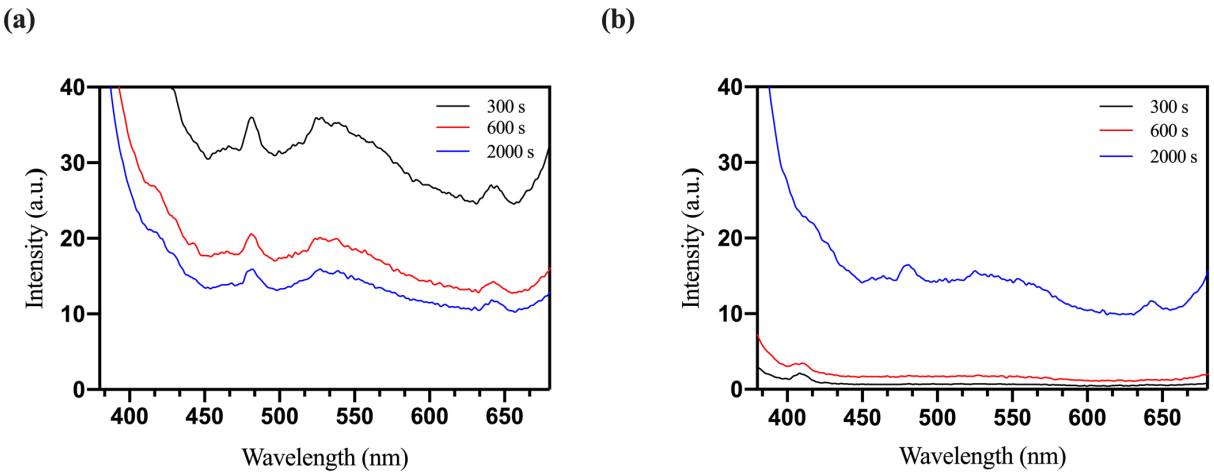

Figure 18. Emission spectra of ZnO electrodeposited at 80 ºC with applied potential of (a) -1.0 V and (b) -0.8 V.

Bearing in mind the factors that influence the growth and formation of ZnO nanorods discussed in previous sections, Figure 19 (a) and (b) summarizes the results that correspond for the optical properties of ZnO nanorods. Therefore, it is concluded the condition of -1.0 V during 600 s at 80 ºC generates the nanorods with the higher absorption intensity, presence of typical absorption and emission bands, and band gap of 3.35 eV.

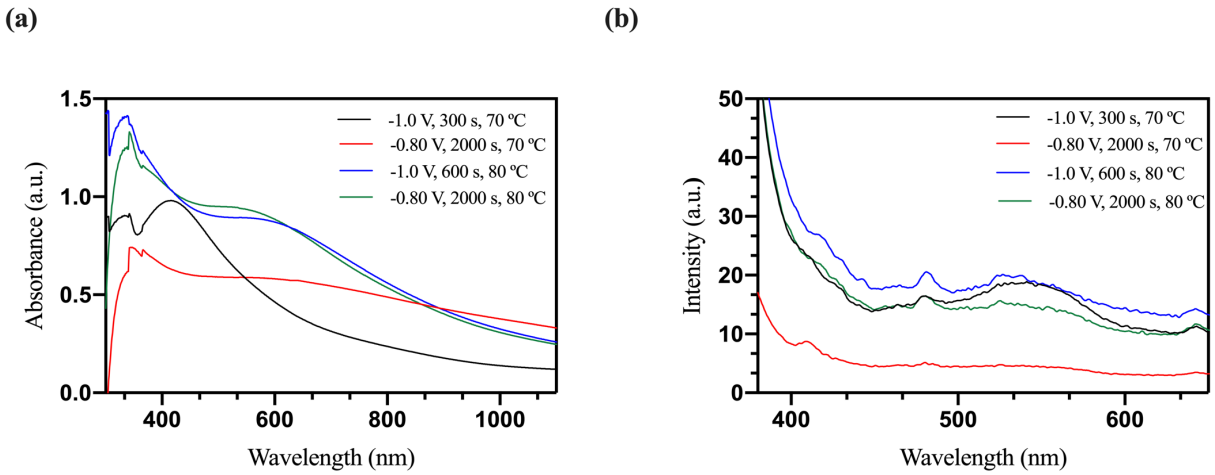

Figure 19. Summary of ZnO experiments.

Figure 20 shows the FE-SEM micrographs of ZnO nanorods electrodeposited on ITO glass slide. Figure 20 shows uniform ZnO nanorods with typical and well-defined hexagonal shape. The nanorods in Figure 20 (a) are about 88 nm to 110 nm in diameter, and are perpendicular to the substrate. The nanorods in Figure 20 (b) exhibit an average diameter of around 285 nm to 315 nm. The diameter and length can be tuned by the electrochemical parameters as the applied potential and deposition time.

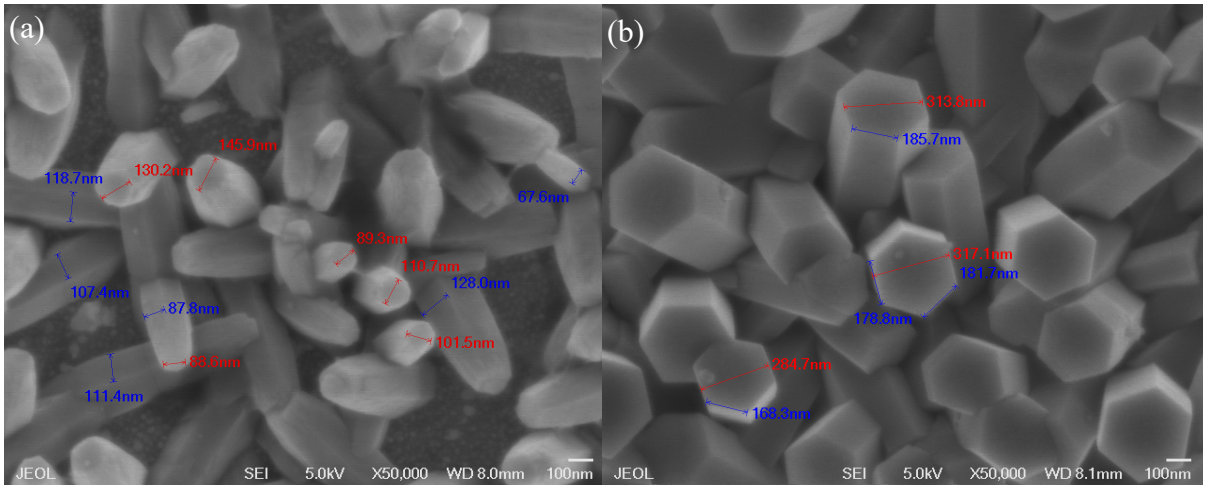

Figure 20. SEM images of ZnO nanorods. (a) -1.0 V, 600 s, 80 ºC and (b) -0.8 V, 2000 s, 70 ºC.

4.2.3 ZnO nanotubes formation

ZnO nanotubes were obtained by the dissolution of ZnO nanorods (Figure 20) in 0.125 M KOH solution at 85 ºC for 20 minutes. The ZnO samples used for the conversion into nanotubes were those obtained at -1.0 V for 600 s at 80 ºC. Figure 21(a) shows ZnO nanotube arrays are randomly oriented since most of them are vertically aligned but the other part lie horizontally with respect to the substrate. By the high-magnification image (Figure 21(b)) reveals the etching process is visible to the bottom of the nanotubes. The conversion of ZnO nanorods into ZnO nanotubes by the etching process conserve the hexagonal shape with a diameter size around 300 nm and a wall thickness approximately of 80 nm. The formation of tubular ZnO is explained by the following etching mechanism proposed by some authors. ZnO exhibits amphoteric characteristic and can be dissolved by acid or alkali solutions, the chemical equations described the process:

$$ZnO + 2OH \rightarrow {ZnO_2}^{2-} + H_2O \quad (16)$$

It is also well-known the {0 0 0 1} plane in ZnO nanostructure has higher surface energy and is metastable that leads to the preferential etch in that plane. Moreover, in the center of nanorods exists more defects that leads to the preferential etch [81, 112].

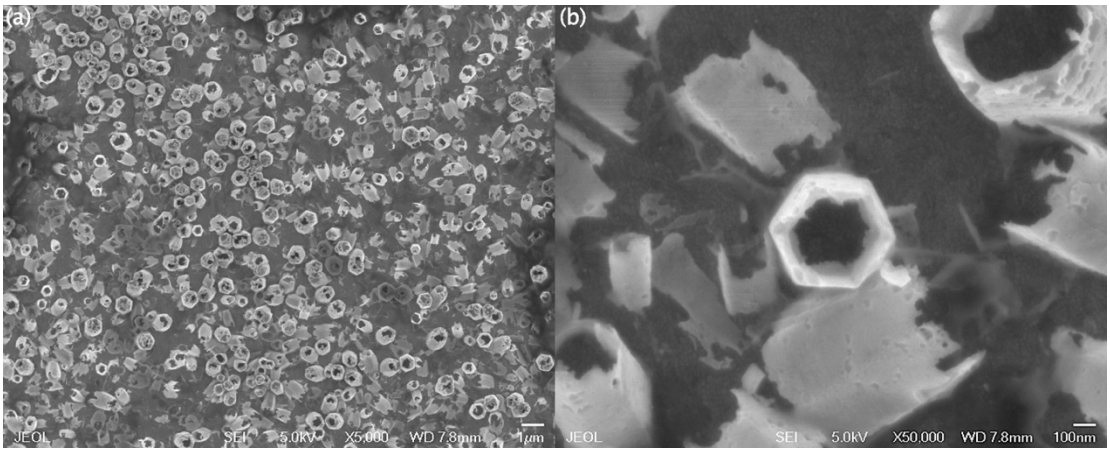

Figure 21. SEM images of ZnO nanotubes. (a) Magnification 5,000X and (b) 50, 000X

4.2.4 Overview: ZnO

The ZnO was obtained in the two different morphologies: nanorods and nanotubes. The hole structure offers the possibility of increasing the interface between ZnO and FeS_2, forming a pn junction and improving properties as the V_{oc} of the hybrid solar cells. The high surface area results in the enhancement of the interfacial area between the ZnO and the P3HT facing the limitations of low electron mobility of the P3HT.

4.3. FeS_2 formation mechanism and characterization

4.3.2 Reaction mechanism of pyrite nanoparticles

Different mechanisms are discussed to drive pyrite formation. In this work, the microwave-assisted synthesis was performed under the reaction mechanism suggested by Wang *et al*. [113]. Briefly, the ethylene glycol in the reaction mixture promotes the formation of S^2 anions and producing precipitated FeS to an aqueous FeS intermediate. The change in the electron density between the central S atom and Fe atoms, leads to the nucleophilic attack of the FeS_{aq} by the S atom, forming a new polysulfide, FeS_2. Alternatively, the formation of H_2S is favorable due to the pH less than 7. The FeS_{aq} reacts with H_2S and forms precipitated FeS_2 [114,115]. Moreover, Ethylene glycol is an excellent solvent with low-toxicity. During the pyrite formation, ethylene glycol avoids the iron oxides formation during the synthesis without the need of an inert atmosphere.

$$2HOCH_2CH_2OH \rightarrow 2CH_3CHO + H_2O \quad (17)$$

$$2CH_3CHO + S \rightarrow CH_3CO - COCH_3 + H_2S \quad (18)$$

$$H_2S \leftrightharpoons HS^- + H^+ \quad (19)$$

$$HS^- \leftrightharpoons S^{2-} + H^+ \quad (20)$$

$$FeS + S_n^{2-} \rightarrow FeS_2 + S_{n-1}^{2-}H^+ \quad (21)$$

$$FeS + H_2S \rightarrow FeS_2 + H_2 \quad (22)$$

It is well known FeS_2 (pyrite) tends to react with O_2 to form different iron oxides on the surface of the nanomaterial, which causes the diminishing of the photovoltaic properties once the pyrite is incorporated to a solar cell. Taking into consideration the presence of impurities after a period of time, it was established the evaluation of the optical properties (absorption and emission spectra) in order to study its stability with the presence of sodium citrate and sodium tartrate as stabilizers.

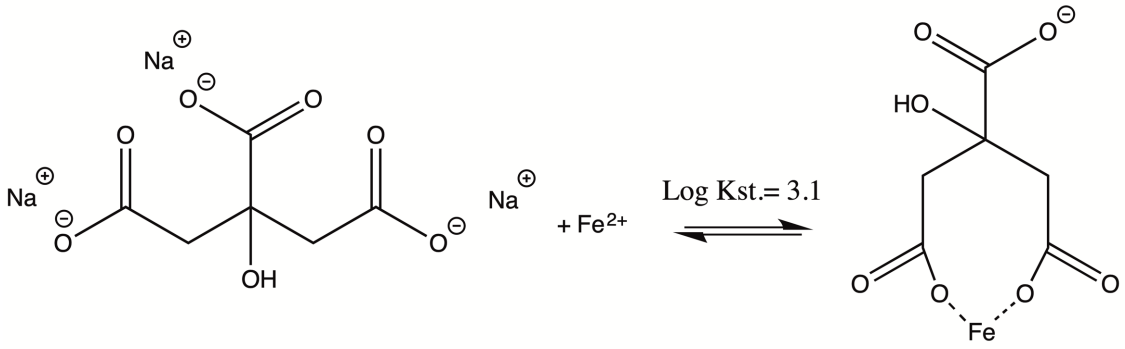

Sodium citrate **Iron (II) citrate complex**

Sodium tartrate **Iron (II) tartrate complex**

Figure 22. Schematic illustration of iron complexes.

Mechanism of the synthesis of FeS_2 via complex agents is based on the previous reactions and the formation of iron-stabilizer complex. In the first-stage a complex of iron-citrate or iron-tartrate is formed. In the case of ferrous iron formed a tridentate complex with citrate ion, $[Fe(II)cit]^-$ involving two carboxylic acid groups and the hydroxyl group [116,117]. In contrast, ferrous iron formed a monodentate complex with tartrate ion, [Fe(II)tar] (Figure 22). The complex stability increases in the order tartrate < citrate [118]. The formation mechanism now depends on the competition between metal-complex formation and the sulfur precipitation, where the last one predominates.

4.3.3 Characterization of FeS_2

Initially, it was studied the structural properties followed by the optical and morphological characterization of the powders. X-ray Diffraction revealed the crystal lattice of the dried FeS_2 powders. Figure 23 shows diffraction pattern for the as-prepared FeS_2 for 150 s of total heating and without the presence of complexing agents. Main characteristic reflection peaks of pyrite are observed at 28.5º, 32.9º, 37.1º, 40.8º, 47.3º and 56.3º for (111), (200), (210), (211), (220) and (311) planes, respectively. All the peaks correspond to a pure cubic system of FeS2 (PDF card 01-071-3840) with a lattice parameter of a= 5.416 Å. Additional peaks for impurities as FeS (troilite) or FeS_2 (marcasite) were not detected. The average crystallite size was estimated using

Debye-Scherrer formula, calculated with the strongest (200) diffraction peak, is 17.5 ± 2.92 nm.

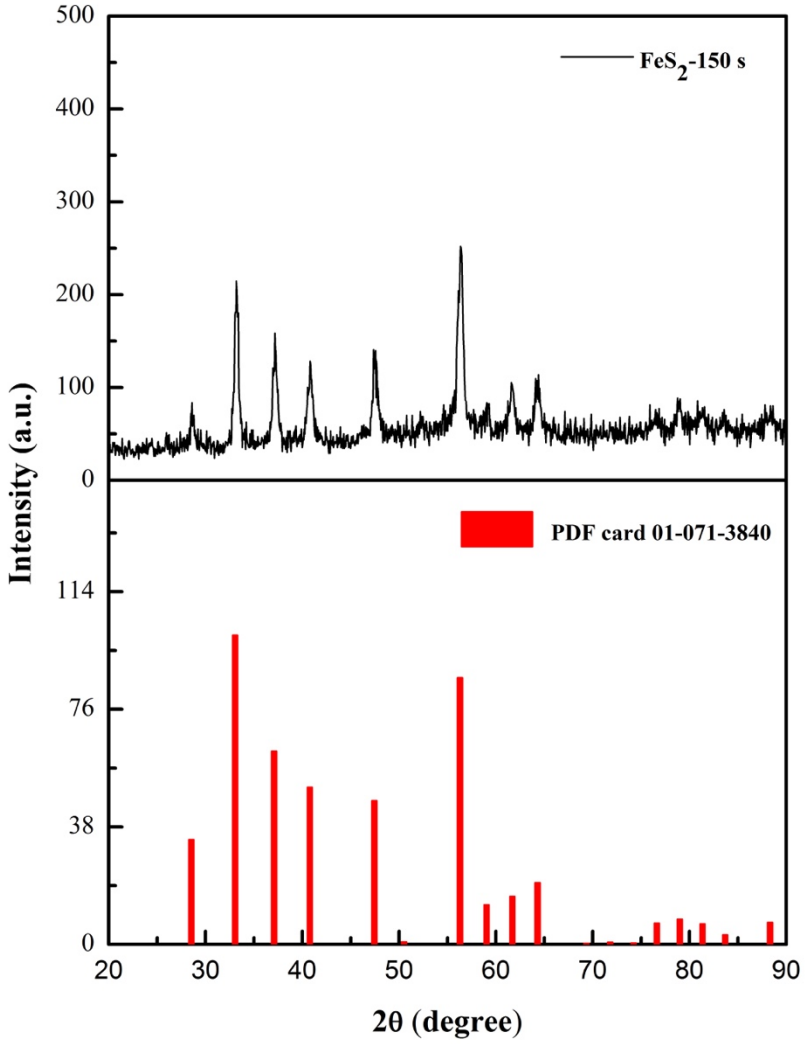

Figure 23. XRD pattern of FeS_2 nanoparticles.

Figure 24 shows the FT-IR spectra of FeS_2, citrate and tartrate capped FeS_2 powders. The broad peak centered around 3495 cm^{-1} is attributed to the strong stretching

vibration of the -OH bond of adsorbed moisture and hydroxyl groups present on the citrate and tartrate anions. Citrate and tartrate ions are present on the surface of the nanoparticles by the peaks at 1650-1700 cm^{-1} are assigned to C=O stretching vibrations of the complexing agents. The peaks around 684-700 cm^{-1} are related to disulfide bond (S-S) [119,120]. The coordination between citrate and tartrate moieties to the surface of the pyrite corresponds with the size distribution of the semiconductors.

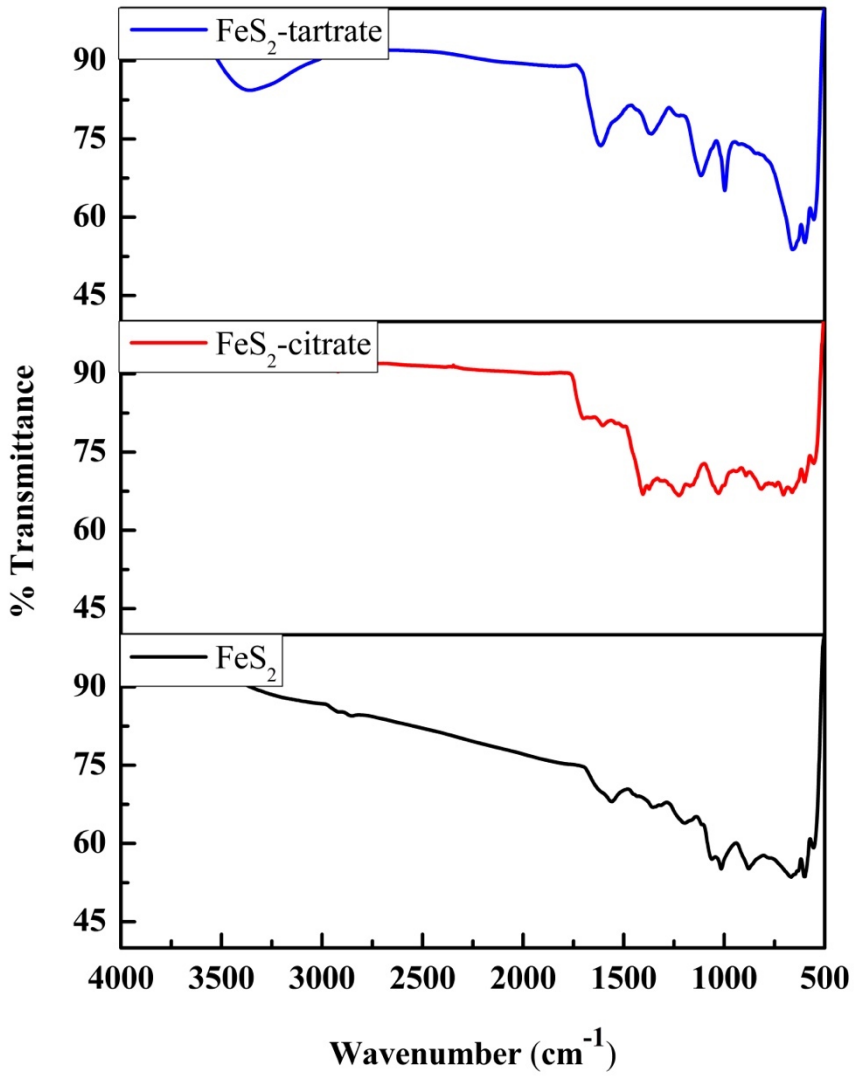

Figure 24. FT-IR spectra of FeS_2 and citrate and tartrate-capped FeS_2 nanoparticles.

FeS_2 nanoparticles were dispersed in ethanol previous analysis. Figure 25 displays the room-temperature absorption spectra of FeS_2 prepared without complexing agents, with tri-sodium citrate, and sodium tartrate. A broad absorbance is observed from 450 to 1100 nm consistent with previous reports in FeS_2 samples. Samples in presence of complexing agents showed the rise of the absorption band around at 900 nm (1.3 eV), which corresponds to the direct bandgap of FeS_2 [121].

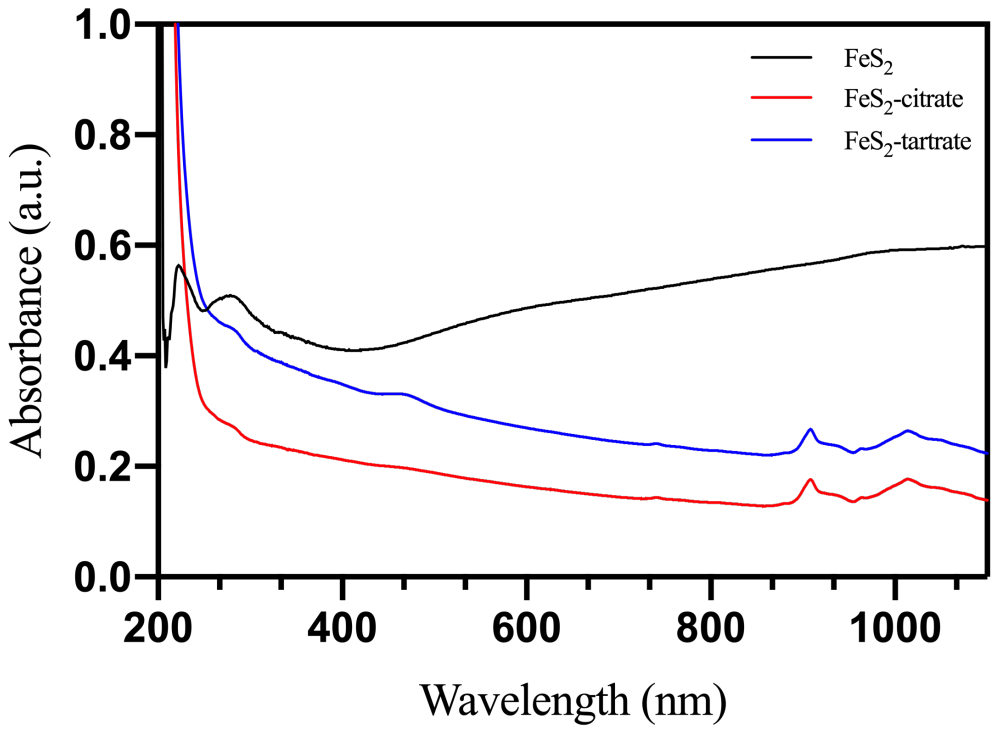

Figure 25. Optical absorption of FeS_2 and citrate and tartrate-capped FeS_2 nanoparticles.

The wide range of optical absorption is characteristic of an electronic structure with broad energy bands. The energy levels in bulk pyrite are a S pσ∗ band and a d-band manifold. The d-band splits into the occupied t_{2g} and the unoccupied e_g sub-bands, with the indirect band gap falling in between. The indistinct boundary between the

S pσ∗ band and e_g subband causes the conduction band to span from 0.95 to 3.65 eV in the bulk [122].

Room temperature photoluminescence of FeS_2 dispersed in ethanol using a 340 nm excitation in the wavelength from 550 nm to 800 nm is shown in Figure 26. PL spectra illustrated two broad emission peaks at 630 and 720 nm, which are assigned to the excited electron-hole recombination from Fe and S atoms while the second band is relative to S-deficient formation, respectively. The S-deficient can be attributed to FeS_2 since it is not a perfect stoichiometric compound, where point defects, surface states, and bulk defects are common in the crystal structure, which can induce unusual PL emissions [123].

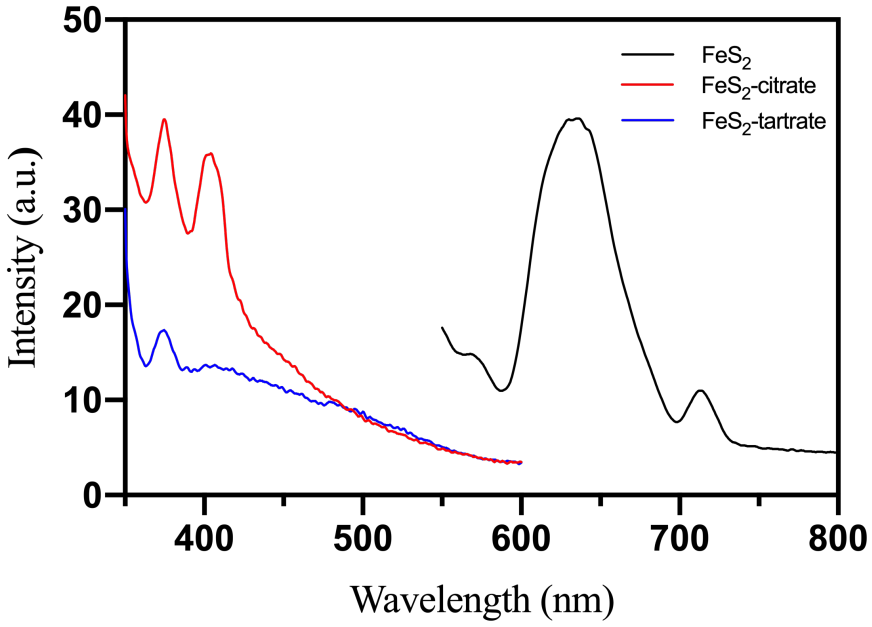

Figure 26. PL spectra of Optical absorption of FeS_2 and citrate and tartrate-capped FeS_2 nanoparticles.

As a photovoltaic material, it is important to notice that a high PL intensity indicates a higher recombination rate of the electro-hole pairs and short lifetime of the photoluminescence state. Figure 26 shows the PL spectra collected from the two complexing agents. It is observed a significant change in position and narrowness of the emission bands in PL spectra attributed to the nanostructure sizes are affected by the citrate and tartrate ions. In addition, it is observed that for tartrate samples the emission intensity is lower than citrate samples, which is attributed to the better crystalline quality of FeS_2-tartrate samples.

Figure 27 (a-c) shows FE-SEM images to reveal morphology and size distribution of FeS_2, Figure 27 (a) shows flower sheet-like FeS_2 morphology with a diameter of 35 nm to 65 nm. While in the presence of sodium citrate and tartrate, it is observed the change of morphology from irregular shape into spherical particles. In Figure 27 (b) particles shows good uniformity with a size distribution of 15 nm to 22 nm. On the other hand, Figure 27 (c) reveals a size distribution of 25 nm to 30 nm. The different morphology and size between samples can be attributed to the influence of tri-sodium citrate and sodium tartrate on the shape and size of particles [63].

4.3.4 FeS_2 stability in presence of citrate and tartrate ions

Additionally, it was studied the influence of citrate and tartrate ions on the optical properties stability against time without special storage conditions. The presence of

citrate and tartrate ions in the synthesis of FeS_2 nanostructures required longer reaction time of 300 and 360 s. The samples were kept without a special atmosphere and at room temperature during the 21 days. XRD was used to verify the crystal structure and the presence of iron oxides of the powders through 21 days. Typical XRD patterns of cubic FeS_2 are shown in Figure 28. In samples with 300 s of total heating is observed the formation of a second phase of Fe_2O_3. through the time while samples with 360 s of reaction time did not exhibit impurities for 21 days. Therefore, longer reaction time increases the crystallinity of the samples, which could contribute to better stability on the surface of FeS_2 and to avoid the iron oxides formation.

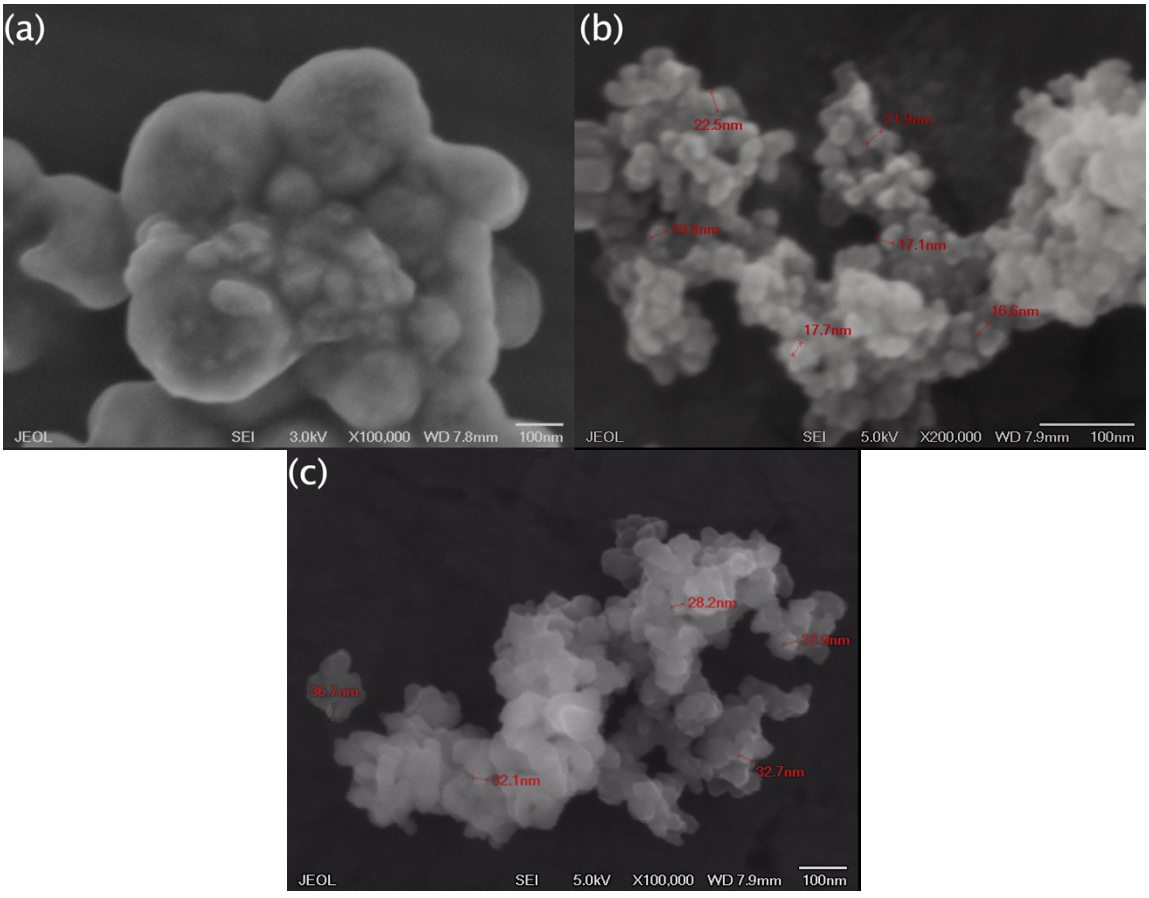

Figure 27. SEM images of (a) FeS_2 nanoparticles and FeS_2 in presence of (b) sodium citrate and (c) sodium tartrate.

Figure 29 (a-d) shows the variation of absorption and emission properties through 21 days. Figure 29 (a-b) corresponds to the absorption decreased of the samples prepared using green stabilizers. Absorption peak positions are consistent through time without evident change in 21 days for FeS_2-citrate samples. In contrast, FeS_2-tartrate showed higher intensity, but the absorption intensity diminished was more significant through the time, which is attributed to the presence of iron oxides. Figure 29 (c-d) shows the PL spectra collected from the two different complex agents. 21 days spectra showed evident changes in the intensity. Emission bands at 420 nm and 500 nm may be attributed or caused by oxygen contamination such as α-Fe_2O_3 (around 440 nm to 500 nm) [124.125]. In addition, it is observed that for tartrate samples the emission intensity is lower than citrate samples, which is attributed to a higher crystalline quality. Additionally, tartrate samples showed higher stability on the emission intensity.

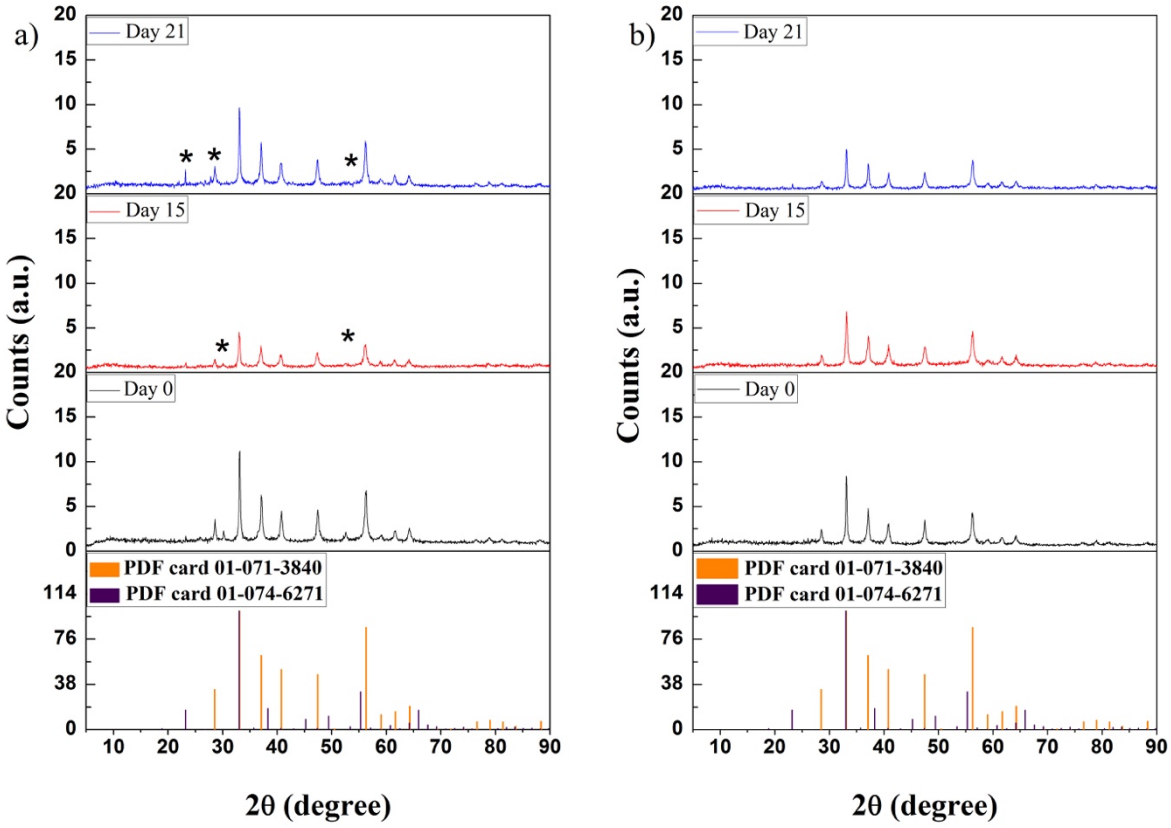

Figure 28. XRD patterns of FeS_2 at (a) 300 s and (b) 360 s of total heating.

Most of the works agree the oxidation on the pyrite surface is due to the incorporation of oxygen on sulfur sites [124], those defects can affect negatively the optoelectronic properties of FeS_2 devices. Previous studies indicate that citrate and tartrate ions are popular complex agents used in the synthesis of semiconductor nanoparticles due to their low toxicity. It is well known, the free electron pairs in the carbonyl groups of the molecules stabilize the nanoparticles by electrostatic forces.

On the basis of the mentioned results it can be inferred that FeS_2 nanoparticles are stabilized by MPA between the interaction of thiol groups [126] while citrate or tartrate ions surround the molecules due to the interaction with carboxyl groups. Although during the days the protection of citrate or tartrate ions is lost due to the presence of oxygen in the atmosphere that leads to a strong interaction between Fe-O atoms that produces Fe_2O_3 [127].

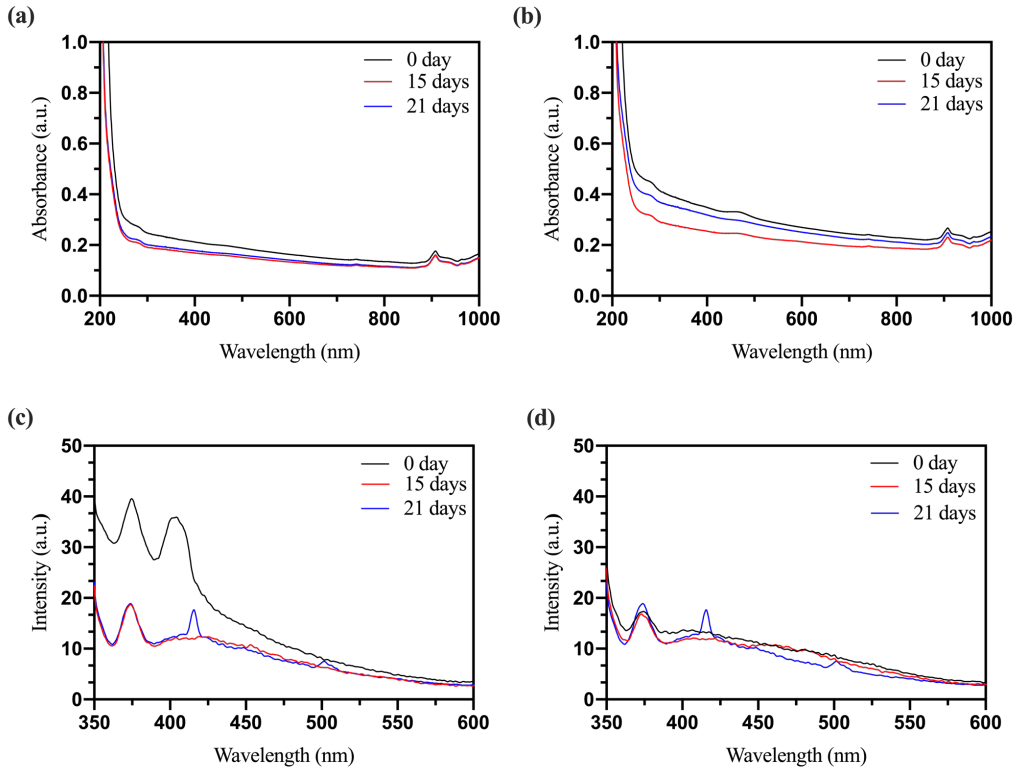

Figure 29. UV-vis spectra of FeS_2 in presence of (a) sodium citrate and (b) sodium tartrate for 21 days. PL spectra of FeS_2 in presence of (c) sodium citrate and (d) sodium tartrate for 21 days.

4.3.5 Overview: Pyrite

The FeS_2 (pyrite) is the most promising absorber material on the basis of optical properties and low-cost. The FeS_2 obtained show absorption in the visible region

modulated by its size and shape, low photoluminescence and no presence of isomorphs. It is been discussed that the enhancement of pyrite properties, especially the optical absorption, can improve the pyrite based solar cells. Moreover, the stability analysis offers additional information about its behavior after the synthesis process without special storage conditions. Therefore, the FeS_2 obtained may overcome the limits in the low open-circuit voltage ($V_{oc} \leq$ 187 mV) and solar conversion efficiency < 3%.

4.4. Hybrid solar cells of FeS_2/ZnO/P3HT

The performance of the hybrid solar cells depends mainly on the photoactive layer configuration due to the exciton formation is promoted by the interface between the donor and acceptor. The inorganic materials worked provide the electron transport improved by pn junction and the high surface area. While the polymeric matrix participates in the hole transport and improves the optical absorption in the visible range. Since the composition of the photoactive layer is already obtained, this layer will be coated with Au in order to study the photovoltaic performance.

Chapter V

Conclusions

Conclusions

Efficient donor P3HT is an important requirement in the enhancement of the performance of the HSC. P3HT thin films were obtained by the electropolymerization of 3-hexylthiophene. The electrochemical oxidative doping of the P3HT makes possible to obtain a semiconductor with suitable structural and optical properties for these devices. It is demonstrated the P3HT thin films exhibited a wide light absorption improved due to strong intrachain interactions along the backbone, called π-π stacking. The applied potential did not cause a change in the P3HT structure. On the other hand, the electrical parameters such as deposition time and cathodic potential can influence the formation of different nanostructures.

ZnO nanorods were grown on ITO-coated glass by electrochemical deposition. This controllable method allowed to obtain vertical aligned arrays of ZnO nanorods under the influence of parameters such as bath temperature, applied potential and deposition time. These parameters can also modify diameter and length aspect ratio. On the other hand, the ZnO nanorods conversion into nanotubes depends on the etching time and the metastability of the { 0 0 0 1} crystal plane along the c-axis. ZnO nanorods show a typical strong absorption in the UV region and weaker absorption in the visible range. The low PL intensity diminishes the exciton recombination. It is expected the one-dimensional ZnO nanoarrays enhance the HSC performance due to the special morphology and intrinsic properties.

A rapid strategy has been used to obtain cubic FeS_2 (pyrite) using complexing agents through microwave-assisted method. The air-stable FeS_2 nanoparticles exhibited a band gap around 1.3 eV showing a broad absorption peak in visible range. Emission spectra indicate the presence of two broad peaks related to a non-stoichiometric compound. The stability study suggests the longer reaction time prevents the oxidation through time, while the presence of sodium citrate allows the formation of smaller particles of FeS_2. Moreover, FeS_2-tartrate samples exhibit better stability behavior compared with FeS_2-citrate samples due to the size influencing the absorption and emission properties. This method offers an opportunity to synthesis other air-stable metal chalcogenides of pyrite chemical family without the need of special storage conditions.

The structural, optical and morphological properties of the semiconductors obtained allow to face the current limitations and enhance the photovoltaic properties of the pyrite-based solar cells.

Future outlook

- Determination of the stoichiometries of Fe-based semiconductors through total-composition techniques as ICP-OES and AAS.
- Electrochemical study of hybrid thin films of FeS_2/ZnO/P3HT through CV, EIS and Mott-Schottky analysis.
- Design and study of the photovoltaic properties of the hybrid solar cells.

References

[1] M.B. de la Mora, O. Amelines-Sarria, B.M. Monroy, C.D. Hernández-Pérez, J.E. Lugo, Materials for downconversion in solar cells: Perspectives and challenges, ***Sol. Energy Mater. Sol. Cells.*** 165 (2017) 59–71. doi:10.1016/j.solmat.2017.02.016.

[2] M.C. Beard, J.M. Luther, A.J. Nozik, The promise and challenge of nanostructured solar cells, ***Nat. Nanotechnol.*** 9 (2014) 951–954. doi:10.1038/nnano.2014.292.

[3] E. Płaczek-Popko, Top PV market solar cells 2016, ***Opto-Electronics Rev.*** 25 (2017) 55–64. doi:10.1016/j.opelre.2017.03.002.

[4] K.D.G.I. Jayawardena, L.J. Rozanski, C.A. Mills, M.J. Beliatis, N.A. Nismy, S.R.P. Silva, "Inorganics-in-Organics": Recent developments and outlook for 4G polymer solar cells, ***Nanoscale.*** 5 (2013) 8411–8427. doi:10.1039/c3nr02733c.

[5] R.W. Miles, G. Zoppi, I. Forbes, Inorganic photovoltaic cells The inorganic semiconductor materials used to make photovoltaic cells, ***Mater. Today.*** 10 (2007) 20–27. doi:10.1016/S1369-7021(07)70275-4.

[6] García Alvarez K. M. Obtention of photoactive Cu-Fe-Sn-S/poly(3-hexylthiophene) hybrid films with potential application in solar cells, Universidad Autónoma de Nuevo León, 2018.

[7] V. Najafi, M. Aghelifar, S. Kimiagar, A novel synthesis of CZTS quantum dots using pulsed laser irradiation, ***Superlattices Microstruct.*** 109 (2017) 702–707. doi:10.1016/j.spmi.2017.05.063.

[8] P. Yu, S. Qu, C. Jia, K. Liu, F. Tan, Modified synthesis of FeS_2 quantum dots for hybrid bulk-heterojunction solar cells, ***Mater. Lett.*** 157 (2015) 235–238. doi:10.1016/j.matlet.2015.05.033.

[9] C. Wadia, A.P. Alivisatos, D.M. Kammen, Materials Availability Expands the Opportunity for Large-Scale Photovoltaics Deployment, ***Environ. Sci. Technol.*** 43 (2009) 2072–2077.

[10] A.J. McGrath, C. Yu, H. Fiedler, J. Butkus, J.M. Hodgkiss, J.E. Halpert, Dual-Functional Optoelectronic and Magnetic Pyrite/Iron Selenide Core/Shell Nanocrystals, ***J. Phys. Chem. C.*** 121 (2017) 8220–8226. doi:10.1021/acs.jpcc.7b02643.

[11] L.Y. Huang, L. Meng, Crystallographic behavior of FeS_2 films formed on different substrates, ***Mater. Chem. Phys.*** 124 (2010) 413–416. doi:10.1016/j.matchemphys.2010.06.056.

[12] W. Luan, C. Zhang, L. Luo, B. Yuan, L. Jin, Y.S. Kim, Enhancement of the photoelectric performance in inverted bulk heterojunction solid solar cell with inorganic nanocrystals, ***Appl. Energy.*** 185 (2017) 2217–2223. doi:10.1016/j.apenergy.2016.04.042.

[13] I.N. Yakovkin, N. V. Petrova, Influence of the thickness and surface composition on the electronic structure of FeS_2 layers, ***Appl. Surf. Sci.*** 377 (2016) 184–190. doi:10.1016/j.apsusc.2016.03.188.

[14] C. Wadia, Y. Wu, S. Gul, S.K. Volkman, J. Guo, A.P. Alivisatos, Surfactant-assisted hydrothermal synthesis of single phase pyrite FeS_2 nanocrystals, ***Chem. Mater.*** 21 (2009) 2568–2570. doi:10.1021/cm901273v.

[15] S.C. Mangham, M. Alam Khan, M. Benamara, M.O. Manasreh, Synthesis of iron pyrite nanocrystals utilizing trioctylphosphine oxide (TOPO) for photovoltaic devices, ***Mater. Lett.*** 97 (2013) 144–147. doi:10.1016/j.matlet.2013.01.101.

[16] R. Murphy, D.R. Strongin, Surface reactivity of pyrite and related sulfides, ***Surf. Sci. Rep.*** 64 (2009) 1–45. doi:10.1016/j.surfrep.2008.09.002.

[17] C.C. Uhuegbu, Growth and characterization of ternary chalcogenide thin films for efficient solar cells and possible industrial applications, Covenant University, 2007.

[18] A. U. Ubale, S. G. Ibrahim, Structural, Electrical and Optical Properties of Nanostructured $FeCdS_3$ Thin Films Deposited by Chemical Spray Technique: Effect of Complex, ***Int. J. Mater. Chem.*** 2 (2012) 57–64. doi:10.5923/j.ijmc.20120202.03.

[19] R. Hayes, A. Ahmed, T. Edge, H. Zhang, Core-shell particles: Preparation, fundamentals and applications in high performance liquid chromatography***, J. Chromatogr. A.*** 1357 (2014) 36–52. doi:10.1016/j.chroma.2014.05.010.

[20] X. Yan, S. Fan, X. Zhang, X. Ren, Analysis of Critical Dimensions for Nanowire Core-Multishell Heterostructures, ***Nanoscale Res. Lett.*** 10 (2015) 1–7. doi:10.1186/s11671-015-1097-7.

[21] J. Tang, Z. Huo, S. Brittman, H. Gao, P. Yang, Solution-processed core-shell nanowires for efficient photovoltaic cells, ***Nat. Nanotechnol.*** 6 (2011) 568–572. doi:10.1038/nnano.2011.139.

[22] J. Chandrasekaran, D. Nithyaprakash, K.B. Ajjan, S. Maruthamuthu, D. Manoharan, S. Kumar, Hybrid solar cell based on blending of organic and inorganic materials - An overview, ***Renew. Sustain. Energy Rev.*** 15 (2011) 1228–1238. doi:10.1016/j.rser.2010.09.017.

[23] E. Arici, N.S. Sariciftci, Hybrid solar cells, ***Inorg. Chim. Acta.*** 361 (2008) 929–944. doi:10.1016/j.ica.2007.06.042.

[24] M. Wright, A. Uddin, Organic-inorganic hybrid solar cells: A comparative review***, Sol. Energy Mater. Sol. Cells.*** 107 (2012) 87–111. doi:10.1016/j.solmat.2012.07.006.

[25] R. Liu, Hybrid organic/inorganic nanocomposites for photovoltaic cells, ***Materials (Basel).*** 7 (2014) 2747–2771. doi:10.3390/ma7042747.

[26] T. Xu, Q. Qiao, Conjugated polymer – inorganic semiconductor hybrid solar cells, ***Energy Environ. Sci.*** 4 (2011) 2700–2720. doi:10.1039/c0ee00632g.

[27] Z. Chen, X. Du, Q. Zeng, B. Yang, Recent Development and Understanding of Polymer-Nanocrystals Hybrid Solar Cells Zhaolai, ***Mater. Chem. Front.*** 1 (2017) 1502–1513. doi:10.1039/C7QM00022G.

[28] F. Gao, S. Ren, J. Wang, The renaissance of hybrid solar cells: progresses, challenges, and perspectives, ***Energy Environ. Sci.*** 6 (2013) 2020–2040. doi:10.1039/c3ee23666h.

[29] X. Fan, M. Zhang, X. Wang, F. Yang, X. Meng, Recent progress in organic–inorganic hybrid solar cells, ***J. Mater. Chem. A.*** 1 (2013) 8694–8709. doi:10.1039/c3ta11200d.

[30] H. Huang, W. Deng, Introduction to Organic Solar Cells, in: H. Huang, J. Huang (Eds.), Org. Hybrid Sol. Cells, 1st ed., Springer, 2014: pp. 1–18. doi:10.1007/978-3-319-10855-1.

[31] R. a J. Janssen, J.C. Hummelen, N.S. Sariciftci, Polymer-Fullerene Bulk Heterojunction Solar Cells, ***MRS Bull.*** 30 (2005) 33–36. doi:10.1557/mrs2005.6.

[32] C.E. Stanton, S.T. Nguyen, M. Janet, P.E. Laibinis, N.S. Lewis, Semiconductors, in: B. King (Ed.), Encycl. Inorg. Chem., John Wiley & Sons, 2006: pp. 1–16. doi:10.1002/0470862106.ia217.

[33] H. Ding, X. Sheng, Thin-Film III–V Single Junction and Multijunction Solar Cells and Their Integration onto Heterogeneous Substrates, in: Z. Ma, D. Liu (Eds.), Inorg. Flex. Optoelectron., 1st ed., Wiley-VCH, 2019: pp. 177–207.

[34] N. Asim, K. Sopian, S. Ahmadi, K. Saeedfar, M.A. Alghoul, O. Saadatian, S.H. Zaidi, A review on the role of materials science in solar cells, ***Renew. Sustain. Energy Rev.*** 16 (2012) 5834–5847. doi:10.1016/j.rser.2012.06.004.

[35] D.L. Gochnauer, T.H. Gilani, Conduction Mechanism in Electrically Conducting Polymers, ***Am. J. Undergrad. Res.*** 14 (2018) 49–56. doi:10.33697/ajur.2018.006.

[36] T.-H. Le, Y. Kim, H. Yoon, Electrical and Electrochemical Properties of Conducting Polymers, ***Polymers (Basel).*** 9 (2017) 150. doi:10.3390/polym9040150.

[37] R. Kroon, D.A. Mengistie, D. Kiefer, J. Hynynen, J.D. Ryan, L. Yu, C. Müller, Thermoelectric plastics: from design to synthesis, processing and structure–property relationships, ***Chem. Soc. Rev.*** 45 (2016) 6147–6164. doi:10.1039/C6CS00149A.

[38] U. Mehmood, A. Al-Ahmed, I.A. Hussein, Review on recent advances in polythiophene based photovoltaic devices, ***Renew. Sustain. Energy Rev.*** 57 (2016) 550–561. doi:10.1016/j.rser.2015.12.177.

[39] Z. Zhang, Y. Li, Side-chain engineering of high-efficiency conjugated polymer photovoltaic materials, ***Sci. China Chem.*** 58 (2015) 1–19. doi:10.1007/s11426-014-5260-2.

[40] H. Sun, J. Deng, L. Qiu, X. Fang, H. Peng, Recent progress in solar cells based on one-dimensional nanomaterials, ***Energy Environ. Sci.*** 8 (2015) 1139–1159. doi:10.1039/C4EE03853C.

[41] R.O. Al-Kaysi, T.H. Ghaddar, G. Guirado, Fabrication of one-dimensional organic nanostructures using anodic aluminum oxide templates, ***J. Nanomater.*** 2009 (2009) 1–14. doi:10.1155/2009/436375.

[42] T. Sagawa, S. Yoshikawa, H. Imahori, One-Dimensional Nanostructured Semiconducting Materials for Organic Photovoltaics, ***J. Phys. Chem. Lett.*** 1 (2010) 1020–1025. doi:10.1021/jz100065u.

[43] Z. Fan, J.C. Ho, Self-assembly of one-dimensional nanomaterials for cost-effective photovoltaics, 4 (2011) 164–183. doi: 10.1504/IJNP.2011.040507.

[44] S.T. Picraux, J. Yoo, I.H. Campbell, S.A. Dayeh, D.E. Perea, Semiconductor Nanowires for Solar Cells, in: G.C. Yi (Ed.), Semicond. Nanostructures Optoelectron. Devices, Springer-Verlag, 2012: pp. 297–328. doi:10.1007/978-3-642-22480-5.

[45] E.C. Garnett, M.L. Brongersma, Y. Cui, M.D. Mcgehee, Nanowire Solar Cells, ***Annu. Rev. Mater. Res.*** 41 (2011) 269–295. doi:10.1146/annurev-matsci-062910-100434.

[46] O. Gaute, B. Magnus, Towards high efficiency nanowire solar cells, ***Nano Today.*** 12 (2017) 31–45. doi:10.1016/j.nantod.2016.10.007.

[47] P.R. Sajanlal, T.S. Sreeprasad, A.K. Samal, T. Pradeep, Anisotropic nanomaterials: structure, growth, assembly, and functions, ***Nano Rev.*** 2 (2011) 5883. doi:10.3402/nano.v2i0.5883.

[48] J. Yuan, A.H.E. Müller, One-dimensional organic-inorganic hybrid nanomaterials, ***Polymer.*** 51 (2010) 4015–4036. doi:10.1016/j.polymer.2010.06.064.

[49] Q. Li, S. Ding, W. Zhu, L. Feng, H. Dong, W. Hu, Recent advances in one-dimensional organic p-n heterojunctions for optoelectronic device applications, ***J. Mater. Chem. C.*** 4 (2016) 9388–9398. doi:10.1039/c6tc03280j.

[50] M. Royo, M. De Luca, R. Rurali, I. Zardo, A review on III – V core – multishell nanowires : growth , properties , and applications, ***J. Phys. D. Appl. Phys.*** 50 (2016) 143001. doi:10.1088/1361-6463/aa5d8e.

[51] Y. Qu, X. Duan, One-dimensional homogeneous and heterogeneous nanowires for solar energy conversion, ***J. Mater. Chem.*** 22 (2012) 16171–16181. doi:10.1039/c2jm32267f.

[52] G. Zangari, Electrodeposition of Alloys and Compounds in the Era of Microelectronics and Energy Conversion Technology, ***Coatings.*** 5 (2015) 195–218. doi:10.3390/coatings5020195.

[53] C.D. Fernández-Solis, A. Vimalanandan, A. Altin, J.S. Mondragón-Ochoa, K. Kreth, P. Keil, A. Erbe, Fundamentals of Electrochemistry, Corrosion and Corrosion Protection Christian, in: P.R. Lang, Y. Liu (Eds.), Soft Matter Aqueous Interfaces, 1st ed., Springer International, 2016: pp. 29–70. doi:10.1007/978-3-319-24502-7.

[54] G. Cao, D. Liu, Template-based synthesis of nanorod, nanowire, and nanotube arrays, ***Adv. Colloid. Interfac.*** 136 (2008) 45–64. doi:10.1016/j.cis.2007.07.003.

[55] W. Lee, S.-J.S.S. Park, Porous anodic aluminum oxide: anodization and templated synthesis of functional nanostructures, ***Chem. Rev.*** 114 (2014) 7487–7556. doi:10.1021/cr500002z.

[56] İ. Şişman, Template-Assisted Electrochemical Synthesis of Semiconductor Nanowires, in: A. Hashim (Ed.), Nanowires - Implementations Appl., 1st ed., InTech, 2011: pp. 41–58. doi: 10.5772/20551

[57] A. Santos, T. Kumeria, D. Losic, Nanoporous anodic alumina: A versatile platform for optical biosensors, ***Materials (Basel).*** 7 (2014) 4297–4320. doi:10.3390/ma7064297.

[58] A. Ennaoui, S. Fiechter, W. Jaegermann, H. Tributsch, Photoelectrochemistry of Highly Quantum Efficient Single- Crystalline n-FeS (Pyrite), ***J. Electrochem. Sci. Technol.*** 133 (1986) 97–106. doi:10.1149/1.2108553.

[59] Y.-Y. Lin, D.-Y. Wang, H.-C. Yen, H.-L. Chen, C.-C. Chen, C.-M. Chen, C.-Y. Tang, C.-W. Chen, Extended red light harvesting in a poly(3-hexylthiophene)/iron disulfide nanocrystal hybrid solar cell, ***Nanotechnology.*** 20 (2009) 405-207. doi:10.1088/0957-4484/20/40/405207.

[60] A. Kirkeminde, R. Scott, S. Ren, All inorganic iron pyrite nano-heterojunction solar cells, ***Nanoscale.*** 4 (2012) 7649–7654. doi:10.1039/c2nr32097e.

[61] C. Steinhagen, T.B. Harvey, C.J. Stolle, J. Harris, B.A. Korgel, Pyrite Nanocrystal Solar Cells: Promising, or Fool's Gold?, ***J. Phys. Chem. Lett.*** 3 (2012) 2352–2356. doi: 10.1002/adma.201200753

[62] B.J. Richardson, L. Zhu, Q. Yu, Inverted hybrid solar cells based on pyrite FeS_2 nanocrystals in P3HT:PCBM with enhanced photocurrent and air-stability, ***Sol. Energy Mater. Sol. Cells.*** 116 (2013) 252–261. doi:10.1016/j.solmat.2013.05.014.

[63] S. Middya, A. Layek, A. Dey, P.P. Ray, Synthesis of nanocrystalline FeS_2 with increased band gap for solar energy harvesting, ***J. Mater. Sci. Technol.*** 30 (2014) 770–775. doi:10.1016/j.jmst.2014.01.005.

[64] M. Alam Khan, J.C. Sarker, S. Lee, S.C. Mangham, M.O. Manasreh, Synthesis, characterization and processing of cubic iron pyrite nanocrystals in a photovoltaic cell, ***Mater. Chem. Phys.*** 148 (2014) 1022–1028. doi:10.1016/j.matchemphys.2014.09.013.

[65] L. Luo, W. Luan, B. Yuan, C. Zhang, L. Jin, High Efficient and Stable Solid Solar Cell: Based on FeS_2 Nanocrystals and P3HT: PCBM, ***Energy Procedia.*** 75 (2015) 2181–2186. doi:10.1016/j.egypro.2015.07.368.

[66] A. Matus, A. Ricardo, A. Mendoza, F. De Moure, F. Sandra, A. Mayén, H. Ma, L. Olvera, M. Concepción, A. Arrocena, J. Santos, Poly‐3‐hexylthiophene doped with iron disulfide nanoparticles for hybrid solar cells, Int. J. Energy Res. (2019) 1‐9. doi:10.1002/er.4527.

[67] D.Y. Wang, Y.T. Jiang, C.C. Lin, S.S. Li, Y.T. Wang, C.C. Chen, C.W. Chen, Solution-processable pyrite FeS_2 nanocrystals for the fabrication of heterojunction photodiodes with visible to NIR photodetection, ***Adv. Mater.*** 24 (2012) 3415–3420. doi:10.1002/adma.201200753.

[68] A.J. Mcgrath, C. Yu, H. Fiedler, J.M. Hodgkiss, J.E. Halpert, Dual-Functional Optoelectronic and Magnetic Pyrite/Iron Selenide Core/Shell Nanocrystals, ***J. Phys. Chem. C.*** 121 (2017) 8220–8226. doi:10.1021/acs.jpcc.7b02643.

[69] J.M. Rhodes, J.R. Mcbride, J.E. Macdonald, Synthesis of FeS_2-CoS_2 core-frame and core-shell hybrid nanocubes, ***Chem. Mater.*** 30 (2018) 8121–8125. doi:10.1021/acs.chemmater.8b04491.

[70] T. Ghrib, M.A. Al-messiere, A.L. Al-otaibi, Synthesis and Characterization of ZnO/ZnS Core / Shell Nanowires, ***J. Nanomater.*** 2014 (2014) 1–8. doi: 10.1155/2014/989632.

[71] Z. He, Y. Xia, B. Tang, X. Jiang, J. Su, Fabrication and photocatalytic property of ZnO/Cu_2O core-shell nanocomposites, ***Mater. Lett.*** 184 (2016) 148–151. doi:10.1016/j.matlet.2016.08.020.

[72] F. Retana, FeS_2/ZnO core/shell nanowires: structural, optical and electrochemical properties, Universidad Autónoma de Nuevo León, 2017.

[73] H. Fan, H. Yu, Y. Zhang, J. Guo, Z. Wang, H. Wang, N. Zhao, Y. Zheng, C. Du, Z. Dai, Q. Yan, J. Xu, 1D to 3D hierarchical iron selenide hollow nanocubes assembled from $FeSe_2$@C core-shell nanorods for advanced sodium ion batteries, ***Energy Storage Mater.*** 10 (2017) 48–55. doi:10.1016/j.ensm.2017.08.006.

[74] H. Xu, H. Brismar, Y. Fu, Influence of surface states on blinking characteristics of single colloidal CdSe-CdS/ZnS core-multishell quantum dot, ***J. Colloid Interface Sci.*** 505 (2017) 528–536. doi:10.1016/j.jcis.2017.06.046.

[75] B. Sun, Y. Hao, F. Guo, Y. Cao, Y. Zhang, Y. Li, D. Xu, Fabrication of poly(3-hexylthiophene)/CdS/ZnO core-shell nanotube array for semiconductor-sensitized solar cell, ***J. Phys. Chem. C.*** 116 (2012) 1395–1400. doi:10.1021/jp206067m.

[76] R. Parize, A. Katerski, I. Gromyko, L. Rapenne, E. Karber, E. Appert, M. Krunks, V. Consonni, A ZnO/TiO_2/Sb_2S_3 Core Shell Nanowire Heterostructure for

Extremely Thin Absorber Solar Cells, ***J. Phys. Chem. C.*** 18 (2017) 9672–9680. doi:10.1021/acs.jpcc.7b00178.

[77] R. Xiao, S. Il Cho, R. Liu, S.B. Lee, Controlled Electrochemical Synthesis of Conductive Polymer Nanotube Structures Controlled Electrochemical Synthesis of Conductive Polymer Nanotube Structures, ***J. Am. Chem. Soc.*** 129 (2007) 4483–4489. doi:10.1021/ja068924v.

[78] S. Yilmaz, İ. Polat, M. TomakİN, A. Ünverdİ, Enhanced efficiency of CdS/P3HT hybrid solar cells via interfacial modification, ***Turkish J. Phys.*** 43 (2019) 116–125. doi:10.3906/fiz-1810-21.

[79] Y.H. Lee, M. Ha, I. Song, J.H. Lee, Y. Won, S. Lim, H. Ko, J.H. Oh, High-Performance Hybrid Photovoltaics with Efficient Interfacial Contacts between Vertically Aligned ZnO Nanowire Arrays and Organic Semiconductors, ***ACS Omega.*** 4 (2019) 9996–10002. doi:10.1021/acsomega.9b00778.

[80] D. Pourjafari, T. Serrano, B. Kharissov, Y. Peña, I. Gómez, Template assisted synthesis of poly(3-hexylthiophene) nanorods and nanotubes: growth mechanism and corresponding band gap, ***Int. J. Mater. Res.*** 105 (2015) 414–420. doi:10.3139/146.111196.

[81] G. She, X. Zhang, W. Shi, X. Fan, J.C. Chang, Electrochemical/chemical synthesis of highly-oriented single-crystal ZnO nanotube arrays on transparent conductive substrates, ***Electrochem. Commun.*** 9 (2007) 2784–2788. doi:10.1016/j.elecom.2007.09.019.

[82] F. Rasouli, A. Rouhollahi, F. Ghahramanifard, Fabrication of silver nanoparticles decorated zinc oxide nanotubes by electrodeposition technique for photoelectrochemical water splitting, ***Mater. Sci. Semicond. Process.*** 93 (2019) 371–378. doi:10.1016/j.mssp.2018.08.004.

[83] M.A. Ansari, S. Mohiuddin, F. Kandemirli, M.I. Malik, Synthesis and characterization of poly(3-hexylthiophene): improvement of regioregularity and energy band gap, RSC Adv. 8 (2018) 8319–8328. doi:10.1039/C8RA00555A.

[84] T. Jarosz, K. Kepska, P. Ledwon, M. Procek, W. Domagala, A. Stolarczyk, Poly(3-hexylthiophene) Grafting and Poly(3-hexylthiophene) Grafting and Molecular Dilution: Study of a Class of Conjugated Graft Copolymers, ***Polymers.*** 11 (2019) 1–32. doi: 10.3390/polym11020205.

[85] J. Jenkins, P. Lee, K. Nebesny, E. Ratcliff, Systematic electrochemical oxidative doping of P3HT to probe interfacial charge transfer across polymer- fullerene interfaces, ***J. Mater. Chem. A.*** 2 (2014) 19221–19231. doi:10.1039/C4TA04319G.

[86] R. Gonçalves, E.C. Pereira, L.F. Marchesi, The overoxidation of poly(3-hexylthiophene) (P3HT) thin film: CV and EIS measurements, ***Int. J. Electrochem. Sci.*** 12 (2017) 1983–1991. doi:10.20964/2017.03.44.

[87] E.L. Ratcliff, J.L. Jenkins, K. Nebesny, N.R. Armstrong, Electrodeposited, “Textured” Poly(3-hexyl-thiophene) (e-P3HT) Films for Photovoltaic Applications, ***Chem. Mater.*** 20 (2008) 5796–5806. doi:10.1021/cm8008122.

[88] W. Plieth, Mass transport, in: W. Plieth (Ed.), Electrochem. Mater. Sci., 1st ed., Elsevier B.V., 2008: pp. 143–169. doi:10.1016/B978-0-444-52792-9.X5001-5.

[89] F. V Molefe, M. Khenfouch, M.S. Dhlamini, B.M. Mothudi, Spectroscopic investigation of charge and energy transfer in P3HT/GO nanocomposite for solar cell applications, ***Adv. Mater. Lett.*** 8 (2017) 246–250. doi:10.5185/amlett.2017.1409.

[90] M.E. Nicho, W. Jaimes, M.E. Rivas-Aguilar, H. Hu, M.A. Quevedo-López, Synthesis of poly (3-hexylthiophene-2,5-diyl) in presence of CdS nanoparticles: microscopic and spectroscopic studies, ***Rev. Mex. Física.*** 63 (2017) 516–524.

[91] J. De Castro, M. Fonsêca, P. Arruda, Influence of solvent used on oxidative polymerization of Poly(3-hexylthiophene) in their chemical properties, ***Polímeros***. 5169 (2018) 395–399. doi:10.1590/0104-1428.15916.

[92] L. Farouil, F. Alary, E. Bedel-Pereira, J. Heully, Revisiting the Vibrational and Optical Properties of P3HT: A Combined Experimental and Theoretical Study, ***J. Phys. Chem. A***. 122 (2018) 6532–6545. doi:10.1021/acs.jpca.8b03814.

[93] Y. Yao, H. Dong, W. Hu, Ordering of conjugated polymer molecules: recent advances and perspectives, ***Polym. Chem.*** 4 (2013) 5197–5205. doi:10.1039/c3py00131h.

[94] A.A. Hussein, A.A. Sultan, M.T. Obeid, A.T. Abdulnabi, M.T. Ali, Synthesis and Characterization of poly(3-hexylthiophene), ***Int. J. Sci. Eng. Appl. Sci.*** 1 (2015) 33–38.

[95] A. Azizi, M.R. Khelladi, L. Mentar, V. Subramaniam, A study on electrodeposited zinc oxide nanostructures, ***J. Mater. Sci. Mater. Electron.*** 24 (2013) 153–159. doi:10.1007/s10854-012-0973-5.

[96] N. Ait Ahmed, M. Eyraud, H. Hammache, F. Vacandio, S. Sam, N. Gabouze, P. Knauth, K. Pelzer, T. Djenizian, New insight into the mechanism of cathodic electrodeposition of zinc oxide thin films onto vitreous carbon, ***Electrochim. Acta.*** 94 (2013) 238–244. doi:10.1016/j.electacta.2013.01.103.

[97] G. Riveros, D. Ramírez, A. Tello, R. Schrebler, R. Henríquez, H. Gómez, Electrodeposition of ZnO from DMSO solution: Influence of anion nature and its concentration in the nucleation and growth mechanisms, ***J. Braz. Chem. Soc.*** 23 (2012) 505–512. doi:10.1590/S0103-50532012000300018.

[98] M.D. Reyes Tolosa, J. Orozco-Messana, A.N.C. Lima, R. Camaratta, M. Pascual, M.A. Hernandez-Fenollosa, Electrochemical Deposition Mechanism for ZnO Nanorods: Diffusion Coefficient and Growth Models, ***J. Electrochem. Soc.*** 158 (2011) E107–E110. doi:10.1149/0.020111jes.

[99] E. Rayon, C. Ferrer, Electrochemical Deposition of ZnO Nanostructures. Mechanism of Growth, ***J. Nanosci. Nanotechnol.*** 10 (2010) 1371–1375. doi:10.1166/jnn.2010.1855.

[100] A. Cruickshank, S. Tay, B. Illy, C. Dearden, T.S. Jones, M.A. McLachlan, D.W. McComb, D.J. Riley, S. Heutz, M.P. Ryan, Morphological Control of ZnO Nanostructures Electrodeposited on to Molecular Thin Films, ***Chem. Mater.*** 23 (2011) 3863–3870. doi:10.1021/cm200764h.

[101] M. Marie, S. Mandal, O. Manasreh, An Electrochemical Glucose Sensor Based on Zinc Oxide Nanorods, ***Sensors.*** 15 (2015) 18714–18723. doi:10.3390/s150818714.

[102] R. Devaraj, K. Karthikeyan, K. Jeyasubramanian, Synthesis and properties of ZnO nanorods by modified Pechini process, ***Appl. Nanosci.*** 3 (2013) 37–40. doi:10.1007/s13204-012-0072-1.

[103] N.C. Das, S. Biswas, P.E. Sokol, The photovoltaic performance of ZnO nanorods in bulk heterojunction solar cells, ***J. Renew. Sustain. Energy.*** 3 (2011). doi:10.1063/1.3599838.

[104] Z. Wang, X. Qian, J. Yin, Z. Zhu, Large-Scale Fabrication of Tower-like, Flower-like, and Tube-like ZnO Arrays by a Simple Chemical Solution Route, ***Langmuir.*** 20 (2004) 3441–3448. doi:10.1021/la036098n.

[105] G. Jiangfeng, D. Zhaoming, D. Qingping, X. Yuan, Z. Weihua, Controlled Synthesis of ZnO Nanostructures by Electrodeposition Method, ***J. Nanomater.*** 2010 (2010) 1–6. doi:10.1155/2010/740628.

[106] Y. Dai, Y. Zhang, X.M. Pei, W. Chen, Zinc oxide nanorods and their photoluminescence property, ***J. Wuhan Univ. Technol. Sci. Ed.*** 18 (2003) 20–22. doi:10.1007/BF02838449.

[107] D.F. Wang, T.J. Zhang, Study on the defects of ZnO nanowire, ***Solid State Commun.*** 149 (2009) 1947–1949. doi:10.1016/j.ssc.2009.07.038.

[108] A.B. Djurišić, Y.H. Leung, K.H. Tam, Y.F. Hsu, L. Ding, W.K. Ge, Y.C. Zhong, K.S. Wong, W.K. Chan, H.L. Tam, K.W. Cheah, W.M. Kwok, D.L. Phillips,

Defect emissions in ZnO nanostructures, ***Nanotechnology.*** 18 (2007). doi:10.1088/0957-4484/18/9/095702.

[109] W. Li, Y. Sun, J. Xu, Controllable Hydrothermal Synthesis and Properties of ZnO Hierarchical Micro/Nanostructures, ***Nano-Micro Lett.*** 4 (2012) 98–102. doi:10.3786/nml.v4i2.p98-102.

[110] G.Z. Wang, N.G. Ma, C.J. Deng, P. Yu, C.Y. To, N.C. Hung, M. Aravind, D.H.L. Ng, Large-scale synthesis of aligned hexagonal ZnO nanorods using chemical vapor deposition, ***Mater. Lett.*** 58 (2004) 2195–2198. doi:10.1016/j.matlet.2004.01.020.

[111] A. Goux, T. Pauporté, J. Chivot, D. Lincot, Temperature effects on ZnO electrodeposition, ***Electrochim. Acta.*** 50 (2005) 2239–2248. doi:10.1016/j.electacta.2004.10.007.

[112] J. Yang, Y. Lin, Y. Meng, Y. Liu, A two-step route to synthesize highly oriented ZnO nanotube arrays, ***Ceram. Int.*** 38 (2012) 4555–4559. doi:10.1016/j.ceramint.2012.02.033.

[113] D.-W. Wang, Q.-H. Wang, T.-M. Wang, Controlled growth of pyrite FeS_2 crystallites by a facile surfactant-assisted solvothermal method, ***CrystEngComm.*** 12 (2010) 755–761. doi:10.1039/b917941k.

[114] J. Thiel, J.M. Byrne, A. Kappler, B. Schink, M. Pester, Pyrite formation from FeS and H_2S is mediated through microbial redox activity, ***Proc. Natl. Acad. Sci.*** 116 (2019) 6897–6902. doi:10.1073/pnas.1814412116.

[115] A. Gartman, G.W.L. Iii, Comparison of pyrite (FeS_2) synthesis mechanisms to reproduce natural FeS_2 nanoparticles found at hydrothermal vents, ***Geochim. Cosmochim. Acta.*** 120 (2013) 447–458. doi:10.1016/j.gca.2013.06.016.

[116] A.J. Francis, C.J. Dodge, Influence of Complex Structure on the Biodegradation of Iron-Citrate Complexes, ***Appl. Environ. Microbiol.*** 59 (1993) 109–113.

[117] D. Wyrzykowski, L. Chmurzyn, Thermodynamics of citrate complexation with Mn^{2+}, Co^{2+}, Ni^{2+} and Zn^{2+} ions, ***J. Therm. Anal. Calorim.*** 102 (2010) 61–64. doi:10.1007/s10973-009-0523-4.

[118] C.F. Timberlake, Iron-Malate and Iron-Citrate Complexes, ***J. Chem. Soc.*** (1964) 5078–5085. doi:10.1039/JR9640005078.

[119] A. Dubey, S.K. Singh, B. Tulachan, M. Roy, G. Srivastava, D. Philip, S. Sarkar, M. Das, Nano iron pyrite (FeS_2) exhibits bi-functional electrode character, ***RSC Adv.*** 6 (2016) 16859–16867. doi:10.1039/C6RA01973K.

[120] M. Khabbaz, M.H. Entezari, Journal of Colloid and Interface Science Simple and versatile one-step synthesis of FeS_2 nanoparticles by ultrasonic irradiation, ***J. Colloid Interface Sci.*** 470 (2016) 204–210. doi:10.1016/j.jcis.2016.02.055.

[121] A. Kirkeminde, B.A. Ruzicka, R. Wang, S. Puna, H. Zhao, S. Ren, Synthesis and optoelectronic properties of two-dimensional FeS_2 nanoplates, ***ACS Appl. Mater. Interfaces.*** 4 (2012) 1174–1177. doi:10.1021/am300089f.

[122] F. Jiang, L.T. Peckler, A.J. Muscat, Phase Pure Pyrite FeS_2 Nanocubes Synthesized Using Oleylamine as Ligand , Solvent , and Reductant, ***Cryst. Growth Des.*** 15 (2015) 3565–3572. doi:10.1021/acs.cgd.5b00751.

[123] M. Lei, R. Zhang, H.J. Yang, Y.G. Wang, Synthesis of well dispersed cobalt disulfide and their photoluminescence and magnetic properties, ***Mater. Lett.*** 76 (2012) 87–89. doi:10.1016/j.matlet.2012.02.009.

[124] J. Hu, Y. Zhang, M. Law, R. Wu, First-principles studies of the electronic properties of native and substitutional anionic defects in bulk iron pyrite, ***Phys. Rev. B - Condens. Matter Mater. Phys.*** 85 (2012) 1–10. doi:10.1103/PhysRevB.85.085203.

[125] J. Wu, L. Liu, S. Liu, P. Yu, Z. Zheng, M. Shafa, Z. Zhou, H. Li, H. Ji, Z.M. Wang, High responsivity photoconductors based on iron pyrite nanowires using sulfurization of anodized iron oxide nanotubes, ***Nano Lett.*** 14 (2014) 6002–6009. doi:10.1021/nl503059t.

[126] H. Zhang, Z. Zhou, B. Yang, M. Gao, The influence of carboxyl groups on the photoluminescence of mercaptocarboxylic acid-stabilized CdTe nanoparticles, ***J. Phys. Chem. B.*** 107 (2003) 8–13. doi:10.1021/jp025910c.

[127] E.C. Dos Santos, J.C. De Mendonça Silva, H.A. Duarte, Pyrite Oxidation Mechanism by Oxygen in Aqueous Medium, ***J. Phys. Chem. C.*** 120 (2016) 2760–2768. doi:10.1021/acs.jpcc.5b10949.

Biographical summary

Ma. Fernanda Retana Betancourt

Candidato para el grado de

Doctor en Ciencias con Orientación en Química de los Materiales

Tesis: Hybrid solar cells of pyrite-based/poly(3-hexylthiophene) core/shell nanowires

Campo de estudio: Química de los Materiales

Datos personales: Nacida en Monterrey, Nuevo León, el 3 de Febrero de 1992

Educación: Egresada de la licenciatura en Química Industrial y la Maestría en Ciencias con Orientación en Química de los Materiales de la Facultad de Ciencias Químicas, UANL.

Experiencia profesional: Profesor de asignatura en la Facultad de Ciencias Químicas, de la Universidad Autónoma de Nuevo León desde 2019.

Chalcogenide Letters Vol. 17, No. 7, July 2020, p. 353 - 360

EFFECT OF COMPLEXING AGENTS ON PROPERTIES AND STABILITY OF FeS_2 NANOPARTICLES

F. RETANA, B. KHARISSOV, Y. PEÑA, I. GÓMEZ, T. SERRANO*
Universidad Autónoma de Nuevo León, Facultad de Ciencias Químicas, Laboratorio de Materiales I, Av. Pedro de Alba s/n, Ciudad Universitaria, C.P. 66455, San Nicolás de los Garza, Nuevo León, México

FeS_2 nanoparticles were prepared by microwave method using tri-sodium citrate and sodium tartrate as complexing agents to study their effect on the optical properties and stability for 21 days without special storage conditions. FeS_2 nanoparticles showed absorption in the visible range with a single-phase of cubic pyrite and crystallite size around 17.5 ± 2.92 nm. Moreover, nanoparticles showed a low photoluminescence intensity. The FT-IR spectra indicate the presence of chemical bonds around the nanoparticles. FE-SEM images showed spherical shape and size distribution in the range of 15-30 nm depending on the complexing agent. The use of complexing agents modifies the size and shape of FeS_2 nanoparticles influencing the tuning of absorption and emission spectra through a period of time.

(Received January 31, 2020; Accepted July 8, 2020)

Keywords: Iron disulfide, Complexing agents, Optical properties, Stability, Microwave synthesis

1. Introduction

The use of surface ligands such as complexing agents in the chalcogenides synthesis are useful to modify shape and size for specific applications. Besides, complexing agents may have an effect on agglomeration, degradation and oxidation of chalcogenides [1], which may affect the optical, morphological and electrical properties. Numerous complexing agents have been reported in the synthesis of semiconductors although are being replaced by non-toxic and low-cost complexing agents such as tri-sodium citrate and sodium citrate.

Tri-sodium citrate and sodium tartrate have been extensively used to produce chalcogenide nanoparticles such as CdS [2], PbS [3], CuS [4] and ZnS [5]. Besides, ternary chalcogenides (e.g. $AgInS_2$ and Zn-Ag-In-S) have been prepared in aqueous medium using complex agents [6]. Tri-sodium citrate and sodium tartrate are complex agents that have pairs of free electrons in the carbonyl group, which stabilizes the semiconductor nanoparticles by electrostatic forces, and also act as a ligand with metallic atoms with free pair of electrons [7-8]. Strong complexing agents play an important role in the synthesis of earth-abundant and stable chalcogenide semiconductors.

FeS_2 has attracted attention as photoactive material due to its abundance, non-toxicity and also, a high annual electricity production potential [9-11]. Moreover, its optical properties such as high absorption coefficient ($\alpha > 10^5$ cm^{-1}), a Shockley-Queisser limit around 31%, , a band gap of 0.95 eV and charge mobility of 360 cm^2 V^{-1} s^{-1} [12-14] make pyrite a promising candidate for high-efficient and low-cost solar cells that can be expanded in the current market.

Despite the advantages, pyrite has showed some limitations within solar cells since the highest conversion efficiency reported is about 3% [15]. A number of reasons keep pyrite out of high efficiency solar cells from sulfur deficiencies to second phases during the synthesis process such as hexagonal troilite (FeS) and orthorrhombic marcasite (FeS_2) with band gaps of 0.04 eV and 0.34 eV, respectively [16-17], and also the iron oxides formation after synthesis. Iron oxides may affect the optical and electrical properties of FeS_2 causing a low performance efficiency.

* Corresponding author: tserranoq@uanl.edu.mx

In this work, it is investigated the effect of tri-sodium citrate and sodium tartrate on the morphological, optical properties, and influence on the stability of FeS_2 (pyrite) nanoparticles during 21 days. The formation of long-term stable FeS_2 nanoparticles may provide a path in the generation of high efficient, low-cost and stable solar cells based on earth-abundant semiconductors.

2. Experimental

2.1. Material and reagents

All the chemicals used for the synthesis were analytical grade reagents and used as received. Anhydrous iron (II) chloride (98%) and mercaptopropionic acid (>99 %) were purchased from Sigma Aldrich. Ethylene glycol, acetone (99.7%), ethanol (≥99.8%) and hydrochloric acid (37.4 %)were purchased from DEQ and sodium thiosulfate (99.8%) was obtained from J.T. Baker. Tri-sodium citrate dihydrate (99.3%) and sodium tartrate dihydrate (99.7%) were purchased from Fermont.

2.2. Synthesis of pyrite FeS_2 using green stabilizers

The reaction was carried out as follows. In a vessel, 1 mmol of anhydrous iron chloride (II), 4 mmol of complexing agent (tri-sodium citrate or sodium tartrate) and 4.5 mmol of sodium thiosulfate were mixed with 50 mL of ethylene glycol and kept under magnetic stirring for 15 minutes. Then, 4 mmol mercaptopropionic acid (MPA) were added to the solution under continuous stirring. Finally, 7 mL of deionized water was added. Microwave heating was performed on the reaction mixture in cycles of 10 s ON and 30 s OFF at 100% microwave power (1000 W, 2.45 GHz). Solutions reacted with a total heating time of 360 s. Reaction finalized when grayish-black powder appears. The end product was centrifuged and washed several times with deionized water, ethanol and acetone. In order to purify the black powder was washed with hydrochloric acid 2 N. Finally, the product was dried under N_2 flux at room temperature for 15 minutes. Samples were storage for 21 days without special conditions. Samples were kept at room temperature with 8% humidity.

2.3. Characterization techniques

Crystalline phase and crystallite size of FeS_2 (pyrite) were recorded by X-ray diffraction (XRD) on a Brucker D2 Phaser with a CuKα radiation (Kα= 1.54056 Å). Data were collected by scanning from 5° to 90°. Fourier-Transform Infrared (FT-IR) spectra were acquired using a Perkin Elmer Spectrum Two at room temperature in reflectance mode with a resolution of 4 cm^{-1}. The absorption spectrum and band gap calculation was characterized by ultraviolet-visible spectrophotometer on a Shimadzu UV-1800. The photoluminescence spectra were collected at room temperature on a Perkin Elmer LS55 with an excitation wavelength of 340 nm. The morphology and distribution size of FeS_2 nanoparticles were given by a field emission scanning electron microscope (FE-SEM), JEOL JSM6701F at an accelerating voltage of 3 kV.

3. Results and discussions

3.1. Structural properties

X-ray Diffraction revealed the crystal lattice of the dried FeS_2 powders. Figure 1 shows diffraction pattern for the as-prepared FeS_2 for 150 s of total heating and without the presence of complexing agents. Main characteristic reflection peaks of pyrite are observed at 28.5º, 32.9º, 37.1º, 40.8º, 47.3º and 56.3º for (111), (200), (210), (211), (220) and (311) planes, respectively. All the peaks correspond to a pure cubic system of FeS_2 (PDF card 01-071-3840) with a lattice parameter of a= 5.416 Å. Additional peaks for impurities as FeS (troilite) or FeS_2 (marcasite) were not detected. The average crystallite size was estimated using Debye-Scherrer formula, calculated with the strongest (200) diffraction peak, is 17.5 ± 2.92 nm.

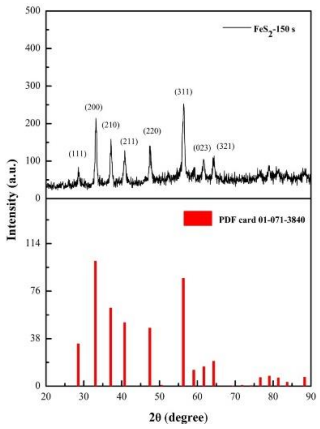

Fig. 1. XRD pattern of FeS_2 nanoparticles.

3.2. FT-IR analysis

Fig. 2 shows the FT-IR spectra of FeS_2, citrate and tartrate capped FeS_2 powders. The broad peak centered around 3495 cm^{-1} is attributed to the -OH stretching mode of water. The peaks at around 1650-1700 cm^{-1} are assigned to C=O stretching vibrations of the complexing agents. The peaks around 684-700 cm^{-1} are related to disulfide bond (S-S) [18-19].

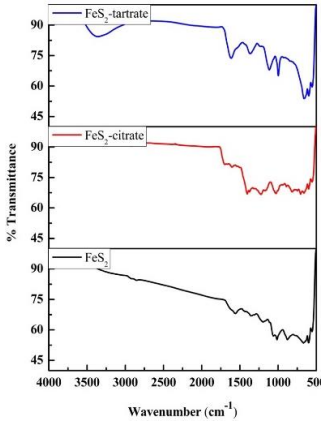

Fig. 2. FT-IR spectra of FeS_2 and citrate and tartrate-capped FeS_2 nanoparticles.

3.3. Optical properties

FeS_2 nanoparticles were dispersed in ethanol previous analysis. Fig. 3 displays the room-temperature absorption spectra of FeS_2 prepared without complexing agents, with tri-sodium citrate, and sodium tartrate. A broad absorbance is observed from 450 to 1100 nm consistent with previous reports in FeS_2 samples. Samples in presence of complexing agents showed the rise of the absorption band around at 900 nm, which corresponds to the direct bandgap of FeS_2 [20]. FeS_2 nanoparticles shows a higher absorption, which affects directly the energy band gap of the nanoparticles. Optical band-gap was estimated with Planck's constant and wavelength (900 nm), for all of samples Eg value is 1.3 eV.

Room temperature photoluminescence of FeS_2 dispersed in ethanol using a 340 nm excitation in the wavelength from 550 nm to 800 nm is shown in Figure 4. PL spectra illustrated two broad emission peaks at 630 and 720 nm, which are assigned to the excited electron-hole recombination from Fe and S atoms while the second band is relative to S-deficient formation, respectively. The S-deficient can be attributed to FeS_2 since it is not a perfect stoichiometric compound, where point defects, surface states, and bulk defects are common in the crystal structure, which can induce unusual PL emissions [21]. As a photovoltaic material, it is important to notice that a high PL intensity indicates a higher recombination rate of the electro-hole pairs and short lifetime of the photoluminescence state. Fig. 4 shows the PL spectra collected from the two complexing agents. It is observed a significant change in position and narrowness of the emission bands in PL spectra attributed to the nanostructure sizes are affected by the citrate and tartrate ions. In addition, it is observed that for tartrate samples the emission intensity is lower than citrate samples, which is attributed to the better crystalline quality.

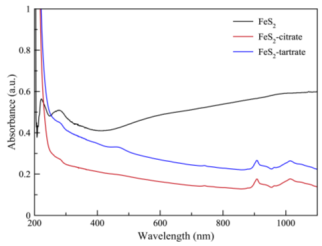

Fig. 3. Optical absorption of FeS_2 and citrate and tartrate-capped FeS_2 nanoparticles.

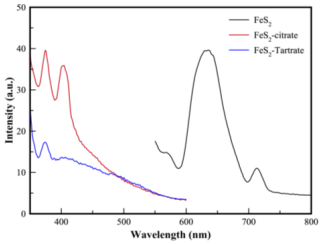

Fig. 4. PL spectra of Optical absorption of FeS_2 and citrate and tartrate-capped FeS_2 nanoparticles.

3.4. FeS_2 morphology

Fig. 5 (a-c) shows FE-SEM images to reveal morphology and size distribution of FeS_2, Fig. 5 (a) shows flower sheet-like FeS_2 morphology with a diameter of 35 nm to 65 nm. While in the presence of sodium citrate and tartrate, it is observed the change of morphology from irregular shape into spherical particles. In Fig. 5 (b) particles shows good uniformity with a size distribution of 15 nm to 22 nm. On the other hand, Fig. 5 (c) reveals a size distribution of 25 nm to 30 nm. The different morphology and size between samples can be attributed to the influence of tri-sodium citrate and sodium tartrate on the shape and size of particles [22].

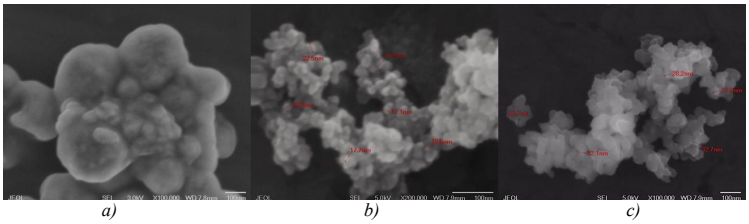

a) *b)* *c)*

Fig. 5. SEM of (a) FeS_2 nanoparticles and FeS_2 in presence of (b) sodium citrate and (c) sodium tartrate.

3.5. FeS_2 stability in presence of citrate and tartrate ions

Additionally, it was studied the influence of citrate and tartrate ions on the optical properties stability against time without special storage conditions. The presence of citrate and tartrate ions in the synthesis of FeS_2 nanostructures required longer reaction time of 300 and 360 s. The samples were kept without a special atmosphere and at room temperature during the 21 days. XRD was used to verify the crystal structure and the presence of iron oxides of the powders through 21 days. Typical XRD patterns of cubic FeS_2 are shown in Fig. 6. In samples with 300 s of total heating is observed the formation of a second phase of Fe_2O_3. through the time while samples with 360 s of reaction time did not exhibit impurities during 21 days. Therefore, longer reaction time increases the crystallinity of the samples, which could contribute to better stability on the surface of FeS_2 and to avoid the iron oxides formation.

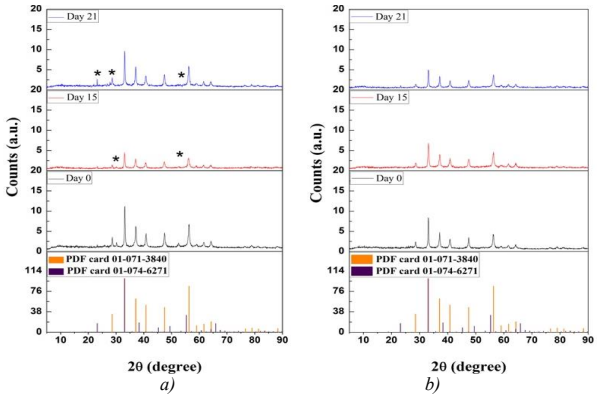

Fig. 6. XRD patterns of FeS_2 at (a) 300 s and (b) 360 s of total heating.

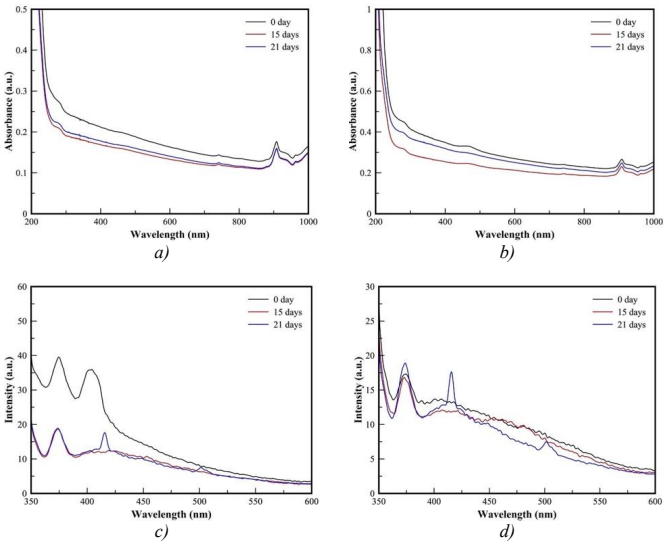

Fig. 7. UV-vis spectra of FeS_2 in presence of (a) sodium citrate and (b) sodium tartrate for 21 days. PL spectra of FeS_2 in presence of (c) sodium citrate and (d) sodium tartrate for 21 days.

Fig. 7 (a-d) shows the variation of absorption and emission properties through 21 days. Fig. 7 (a-b) corresponds to the absorption decreased of the samples prepared using green stabilizers. Absorption peak positions are consistent through time without evident change in 21 days for FeS_2-citrate samples. In contrast, FeS_2-tartrate showed higher intensity but the absorption intensity diminished was more significant through the time, which is attributed to the presence of iron oxides. Fig. 7 (c-d) shows the PL spectra collected from the two different complex agents. 21 days spectra showed evident changes in the intensity, which can be attributed to the presence of iron oxides in the samples. Emission bands at 420 nm and 500 nm corresponds with the typical emission of Fe_2O_3 (around 400 nm to 500 nm) [23]. In addition, it is observed that for tartrate samples the emission intensity is lower than citrate samples, which is attributed to the better crystalline quality. Moreover, tartrate samples showed higher stability on the emission intensity.

Different mechanisms in the reaction of pyrite and oxygen have been investigated. Most of the works agree the oxidation on the pyrite surface is due to the incorporation of oxygen on sulfur sites [24], those defects can affect negatively the optoelectronic properties of FeS_2 devices. Previous studies indicate that citrate and tartrate ions are popular complex agents used in the synthesis of semiconductor nanoparticles due to their low toxicity. It is well known, the free electron pairs in the carbonyl groups of the molecules stabilize the nanoparticles by electrostatic forces.

On the basis of the mentioned results it can be inferred that FeS_2 nanoparticles are stabilized by MPA between the interaction of thiol groups [25] while citrate or tartrate ions surround the molecules due to the interaction with carboxyl groups. Although during the days the protection of citrate or tartrate ions is lost due to the presence of oxygen in the atmosphere that leads to a strong interaction between Fe-O atoms that produces Fe_2O_3 [26].

4. Conclusions

A rapid strategy has been used to obtain cubic FeS_2 (pyrite) using complexing agents through microwave-assisted method. The air-stable FeS_2 nanoparticles exhibited a band gap around 1.3 eV showing a broad absorption peak in visible range. Emission spectra indicate the presence of two broad peaks related to a non-stoichiometric compound.

The stability study suggests the longer reaction time prevents the oxidation through time, while the presence of sodium citrate allows the formation of smaller particles of FeS_2. Moreover, FeS_2-tartrate samples exhibit better stability behavior compared with FeS_2-citrate samples due to the size influencing the absorption and emission properties. This method offers an opportunity to synthesis other air-stable metal chalcogenides of pyrite chemical family without the need of special storage conditions.

Acknowledgements

This research (or network) received funding the Mexican Council for Science and Technology (CONACYT) grant PN150 and the PAICYT (UANL) IT1088-19.

References

[1] Y. Zhang, A. Clapp, Sensors **11**(12), 11036 (2011).
[2] C. Selene Coria-Monroy, M. Sotelo-Lerma, C. Martínez-Alonso, P. M. Moreno-Romero, C. A. Rodríguez-Castañeda, I. Corona-Corona, H. Hu, J. Electron. Mater. **44**(10), 3302 (2015).
[3] P. Zhao, J. Wang, G. Chen, Z. Xiao, J. Zhou, D. Chen, K. Huang, J. Nanosci. Nanotechnol. **8**(1), 379 (2007).
[4] X. Chen, J. Yang, T. Wu, L. Li, W. Luo, W. Jiang, L. Wang, Nanoscale **10**(32), 15130 (2018).
[5] A. K. Thottoli, A. K. A. Unni, J. Nanostructure Chem. **3**(56), 1 (2013).
[6] D. S. Mazing, O. A. Korepanov, O. A. Aleksandrova, V. A. Moshnikov, Opt. Spectrosc. **125**(11), 773 (2018).
[7] A. C. S. Samia, J. A. Schlueter, J. S. Jiang, S. D. Bader, C. J. Qin, X. M. Lin, Chem. Mater. **18**(22), 5203 (2006).
[8] L. C. Königsberger, E. Königsberger, P. M. May, G. T. Hefter, J. Inorg. Biochem. **78**(3), 175 (2000).
[9] C. Wadia, A. P. Alivisatos, D. M. Kammen, Environ. Sci. Technol**. 43**(6), 2072 (2009).
[10] P. S. Vasekar, T. P. Dhakal, in: A. Morales-Acevedo, "Solar Cells. Research and Application Perspectives", Intech Open, UK, 145 (2013).
[11] M. Alam Khan, J. C. Sarker, S. Lee, S. C. Mangham, M. O. Manasreh, Mater. Chem. Phys. **148**(3), 1022 (2014).
[12] M. Cabán-Acevedo, M. S. Faber, Y. Tan, R. J. Hamers, S. Jin, Nano Lett. **12**(4), 1977 (2012).
[13] I. N. Yakovkin, N. V. Petrova, Appl. Surf. Sci. **377**(1), 184 (2016).
[14] M. Wang, C. Xing, K. Cao, L. Zhang, J. Liu, L. Meng, J. Mater. Chem. A. **2**(25), 9496 (2014)
[15] L. Luo, W. Luan, B. Yuan, C. Zhang, L. Jin, Energy Procedia. **75**, 2181 (2015).
[16] R. Murphy, D. R. Strongin, Surf. Sci. Rep. **64**(1), 1 (2009).
[17] S. C. Mangham, M. Alam Khan, M. Benamara, M. O. Manasreh, Mater. Lett. **97**, 144 (2013).
[18] A. Dubey, S. K. Singh, B. Tulachan, M. Roy, G. Srivastava, D. Philip, S. Sarkar, M. Das, RSC Adv. **6**(20), 16859 (2016).
[19] M. Khabbaz, M. H. Entezari, J. Colloid Interface Sci. **470**, 204 (2016).
[20] A. Kirkeminde, B.A. Ruzicka, R. Wang, S. Puna, H. Zhao, S. Ren, ACS Appl. Mater. Interfaces. **4**(3), 1174 (2012).